Probability Distribution Characteristics for Surface Air–Sea Turbulent Heat Fluxes over the Global Ocean

SERGEY K. GULEV

P. P. Shirshov Institute of Oceanology, and Moscow State University, Moscow, Russia, and Institut für Meereskunde-GEOMAR, Kiel, Germany

KONSTANTIN BELYAEV

P. P. Shirshov Institute of Oceanology, Moscow, Russia, and Department of Mathematics, University of Bahia, Salvador, Brazil

(Manuscript received 16 November 2010, in final form 22 May 2011)

ABSTRACT

To analyze the probability density distributions of surface turbulent heat fluxes, the authors apply the two-parametric modified Fisher–Tippett (MFT) distribution to the sensible and latent turbulent heat fluxes recomputed from 6-hourly NCEP–NCAR reanalysis state variables for the period from 1948 to 2008. They derived the mean climatology and seasonal cycle of the location and scale parameters of the MFT distribution. Analysis of the parameters of probability distributions identified the areas where similar surface turbulent fluxes are determined by the very different shape of probability density functions. Estimated extreme turbulent heat fluxes amount to 1500–2000 W m^{-2} (for the 99th percentile) and can exceed 2000 W m^{-2} for higher percentiles in the subpolar latitudes and western boundary current regions. Analysis of linear trends and interannual variability in the mean and extreme fluxes shows that the strongest trends in extreme fluxes (more than 15 W m^{-2} $decade^{-1}$) in the western boundary current regions are associated with the changes in the shape of distribution. In many regions changes in extreme fluxes may be different from those for the mean fluxes at interannual and decadal time scales. The correlation between interannual variability of the mean and extreme fluxes is relatively low in the tropics, the Southern Ocean, and the Kuroshio Extension region. Analysis of probability distributions in turbulent fluxes has also been used in assessing the impact of sampling errors in the Voluntary Observing Ship (VOS)-based surface flux climatologies, allowed for the estimation of the impact of sampling in extreme fluxes. Although sampling does not have a visible systematic effect on mean fluxes, sampling uncertainties result in the underestimation of extreme flux values exceeding 100 W m^{-2} in poorly sampled regions.

1. Introduction

Surface turbulent air–sea fluxes are highly variable over all time scales. Long-term global surface flux time series are available from Voluntary Observing Ship (VOS) data, satellite observations, and reanalyses. Compared to the monthly VOS flux climatologies of Josey et al. (1999) and Grist and Josey (2003), the present-day VOS-based products (e.g., Berry and Kent 2009) provide daily surface fluxes. Daily surface turbulent fluxes for the period from 1985 onward are also available from Woods Hole Oceanographic Institution (WHOI) objectively analyzed air–sea fluxes (OAFlux) climatology (Yu et al. 2004a,b; Yu and Weller 2007), which combines reanalyses and satellite observations by using the variational approach to develop the objectively analyzed flux fields. Surface fluxes and flux-related variables from the global reanalyses are available with 6-hourly resolution. However, in most cases these flux datasets as well as satellite-based turbulent flux products (e.g., Chou et al. 2004; Bouras 2006; Bentamy et al. 2003; Grodsky et al. 2009; Andersson et al. 2011) are evaluated in terms of the first and second moments of the distribution. At the same time, the detailed evaluation of different products, including their ability to diagnose extreme fluxes, require accurate knowledge of probability density functions (PDFs) of turbulent fluxes.

Characteristics of probability distributions of turbulent fluxes are vital for assessing error variances, analyzing averaged fluxes, and comparing the observed fluxes with climate model estimates. It was demonstrated by A. Romanou (2006, personal communication) that surface fluxes

Corresponding author address: Sergey Gulev, P. P. Shirshov Institute of Oceanology, Russian Academy of Sciences, 36 Nakhimovsky Ave., 117997 Moscow, Russia.
E-mail: gul@sail.msk.ru

DOI: 10.1175/2011JCLI4211.1

simulated by Intergovernmental Panel on Climate Change (IPCC) Fourth Assessment Report (AR4) climate models imply remarkably different global PDFs in comparison with the observations. Smith et al. (2011) showed large differences in various percentiles of surface turbulent fluxes from different datasets, even when the means and medians qualitatively agree with each other. Furthermore, PDFs of surface turbulent fluxes are needed for the accurate analysis of decorrelation scales in surface fluxes (Romanou et al. 2006) and for the estimation of extreme turbulent fluxes, which are strongly localized in space and time.

Case studies (e.g., Yau and Jean 1989; LabSea Group 1998; Bond et al. 2010; Tomita et al. 2010) show that in the mid- and subpolar latitudes, particularly in the western boundary current regions, extreme turbulent fluxes exceeding 1000–2000 W m^{-2} occur at such scales as of tens of kilometers and hours. These extremes are typically associated with the intense synoptic transients experiencing explosive development over the midlatitudinal ocean (Bond and Cronin 2008; Zolina and Gulev 2003; Shaman et al. 2010; Rudeva and Gulev 2011). Quantitative description of these events requires the knowledge of the whole statistical distribution of surface fluxes. This task can hardly be achieved using raw observations, because these events are poorly captured by the VOS observations from the International Comprehensive Ocean–Atmosphere Data Set (ICOADS; Worley et al. 2005; Woodruff et al. 2011).

Characteristics of statistical distributions of surface turbulent fluxes are particularly important for analyzing flux products based on VOS data. The accuracy of the estimation of air–sea turbulent fluxes from the VOS data depends on the uncertainties of parameterizations, biases inherent in meteorological observations, and sampling errors. The quality of parameterizations has largely been improved over the last years, owing to the development of the Coupled Ocean–Atmosphere Response Experiment (COARE) family of algorithms (WGASF 2000; Fairall et al. 2003; Brunke et al. 2003) that guarantee an accuracy of 5 W m^{-2} for a wide range of surface conditions. Uncertainties due to observational errors in variables routinely measured and estimated by VOS (Josey et al. 1999; Brohan et al. 2006; Kent and Berry 2005) amount to ± 15 W m^{-2} and can be significantly minimized now by incorporating metadata into the ICOADS collection (Worley et al. 2005; Kent et al. 2007; Woodruff et al. 2011). However, VOS-based air–sea fluxes and flux-related variables are also influenced by sampling errors (Lo and McBean 1978; Weare and Strub 1981; Weare 1989; Legler 1991; Cayan 1992; Gleckler and Weare 1997; Sterl 2001; Kaplan et al. 2003; Smith and Reynolds 2004; Brohan et al. 2006; Kent and Berry 2005; Chang 2005, 2007). Gulev et al. (2007a,b) provided comprehensive estimates of different sources of sampling uncertainties in the VOS-based surface fluxes using reanalyses that were subsampled to simulate the actual VOS sampling density. They reported sampling errors in the turbulent heat fluxes of up to 30–80 W m^{-2} in some poorly sampled regions. These may exceed the uncertainties associated with parameterizations and variable corrections. Furthermore, time-dependent sampling uncertainties may seriously affect estimates of secular changes and interannual variability in surface turbulent fluxes (Gulev et al. 2007b). Further quantification and minimization of sampling errors in the VOS-based surface flux estimates requires knowledge of probability distribution of fluxes. However, in many regions the limited number of VOS observations does not allow for the determination of statistical distribution characteristics unless the theoretical PDFs for surface turbulent fluxes are justified.

Probability distributions for different marine meteorological variables (temperatures, SLP, precipitation, waves, and winds) are represented by a variety of functions of which the Gaussian, gamma, and Weibull PDFs are most frequently used. For instance, for surface winds, the characteristics of the Weibull distribution were analyzed by Wright and Thompson (1983), Isemer and Hasse (1991), Monahan (2006a,b), and Morrissey et al. (2010). Recently, Monahan (2007) has analyzed some non-Weibull behavior in surface winds and suggested using the maximum entropy distribution for the wind speed at sea. Nevertheless, probability distribution for surface turbulent heat fluxes has not yet been justified. In this paper, we will describe some statistical properties of surface latent and sensible turbulent air–sea fluxes with a modified Fisher–Tippett (MFT) distribution (section 2). The description of data and preprocessing (section 3) is followed by the global climatologies of distribution parameters and those of the turbulent fluxes of rare occurrences (section 4). Characteristics of linear trends and interannual variability in the parameters of surface flux PDFs and in extreme fluxes are presented in section 5. In section 6, we apply distributions of surface fluxes to estimate the impact of sampling in the VOS-based mean and extreme fluxes. Discussion in section 7 presents the potential further applications of the probability distributions of surface turbulent fluxes.

2. Probability density distribution of surface air–sea turbulent heat fluxes

Individual values of surface turbulent fluxes over sea can vary within the range from -300 to 1500 W m^{-2} for the sensible heat flux Q_h and from small negative values to 1500–2000 W m^{-2} for the latent heat flux Q_e with the modal values lying in the range from -50 to about

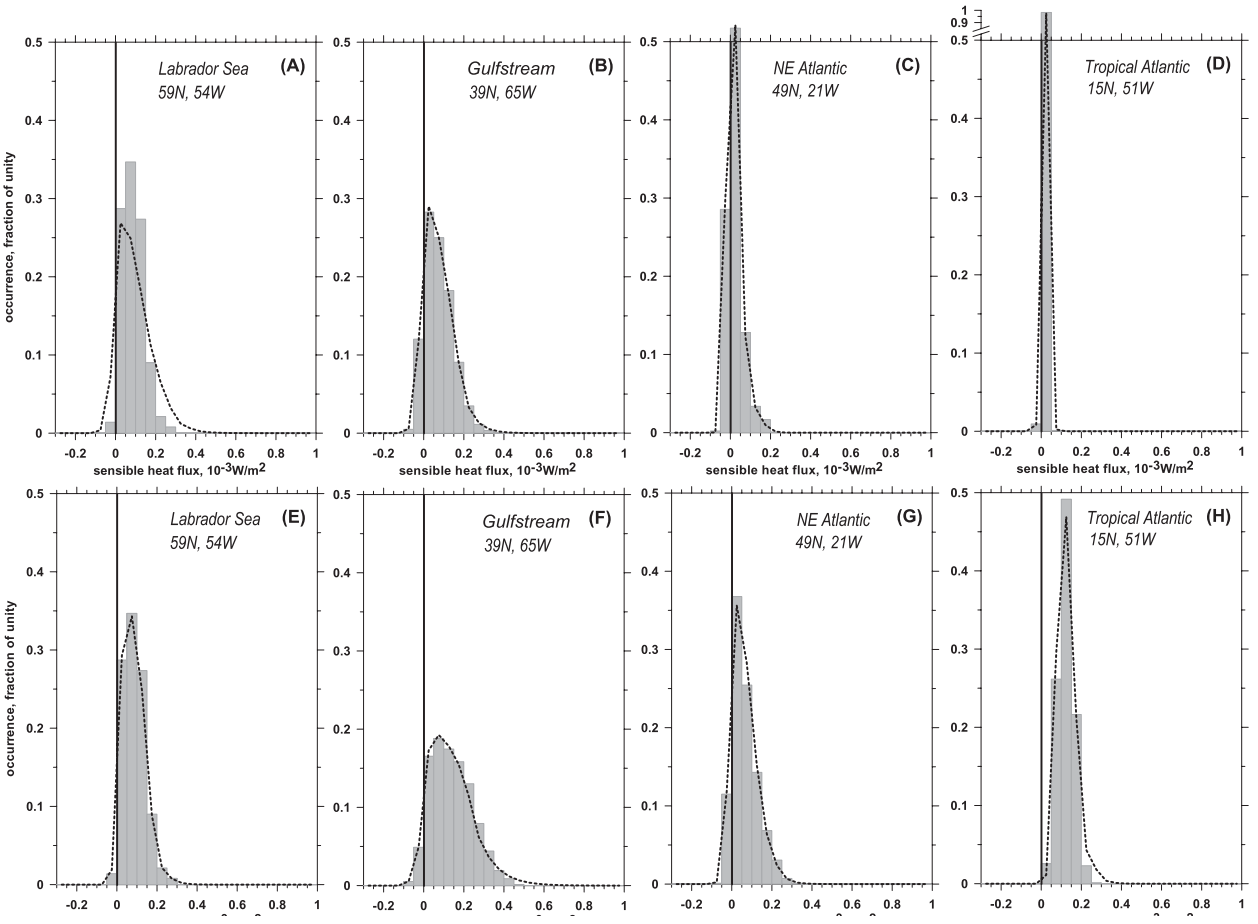

FIG. 1. Empirical occurrence histograms of surface turbulent (top) sensible and (bottom) latent heat fluxes for the winter season (JFM) during the 10-yr period 1992–2001 in the four North Atlantic regions, characterized by different surface meteorological conditions: (a),(e) Labrador Sea, 59°N, 54°W; (b),(f) Gulf Stream, 39°N, 65°W; (c),(g) northeast Atlantic 49°N, 21°W; and (d),(h) tropical Atlantic, 15°N, 51°W. Thick dotted lines show the fits of MFT distribution to each subset.

500 W m^{-2}. The highest turbulent fluxes are observed in the mid- and subpolar latitudes, characterized by the strongest short-period synoptic and mesoscale variability.

Figure 1 shows empirical occurrence histograms of surface turbulent heat fluxes for the winter season [January–March (JFM)] during the 10-yr period between 1992 and 2001 in the four North Atlantic regions characterized by different surface meteorological conditions. These distributions were derived from 6-hourly high-resolution surface fluxes diagnosed by the National Centers for Environmental Prediction–National Center for Atmospheric Research (NCEP–NCAR) reanalysis (Kalnay et al. 1996; Kistler et al. 2001). The Labrador Sea and Gulf Stream are characterized by the strong synoptic variability of surface turbulent fluxes, with the sensible heat flux being dominant in the Labrador Sea and the latent flux prevailing over the Gulf Stream. In the northeast Atlantic, both sensible and latent fluxes are relatively small, with the mean values of about several tens of watts per square meter. The Atlantic tropics show a very small sensible flux and quite strong latent fluxes. In all regions for both Q_h and Q_e, the histograms imply more heavy tails of the distributions for high positive values (positive fluxes are directed to the atmosphere) and thus a strong asymmetry of the PDFs. In some regions distributions of air–sea fluxes can exhibit different skewness and kurtosis. The modal values and long-term means are typically positive, although in some areas they can be negative, as, for example, in the upwelling regions in the eastern subtropics and tropics.

The occurrence histograms in Fig. 1 imply that the distribution of surface turbulent fluxes can be modeled by the family of the Fisher–Tippett distributions (e.g., Besset 2001) as follows:

$$P_T(x) = \beta_T^{-1} \exp\{[(\alpha_T - x)/\beta_T] - \exp[(\alpha_T - x)/\beta_T]\}, \quad (1)$$

where $P_T(x)$ is a probability density function with variable x representing either Q_h or Q_e, and α_T and β_T are

the location and scale parameters, respectively. This distribution is frequently used in various applications of physics of percolation (Bazant 2000), astrophysics (Bhavsar and Barrow 1985), and environmental science (Sayama and Sekine 2001). The Gumbel distribution, frequently applied to the analysis of extreme values, can be derived as a partial case of the Fisher–Tippett distribution. For the analysis of surface turbulent heat fluxes, we will consider a MFT distribution (1) in the following form:

$$P(x) = \alpha\beta \exp(-\beta x) \exp[-\alpha \exp(-\beta x)], \quad (2)$$

where probability density function $P(x)$ is steered by parameters α and β, which are linked to α_T and β_T by the following relationships:

$$\alpha = \exp(\alpha_T/\beta_T) \quad \text{and} \quad \beta = 1/\beta_T. \quad (3)$$

Of the two parameters of PDF (2), α is nondimensional and β holds the dimension of the inversed units of a variable, while in (1) both parameters hold the dimensions. This modification of (1) will provide a better prospect for the further interpretation of the parameters of distribution. Integration of the PDF (2) returns us to the following cumulative distribution function (CDF) $C(x)$:

$$C(x) = \exp[-\alpha \exp(-\beta x)], \quad (4)$$

and to the following expressions for the mean and variance:

$$\overline{x} = \int_{-\infty}^{\infty} P(x)x\,dx = \frac{C + \ln\alpha}{\beta} \quad \text{and}$$

$$\text{var}x = \int_{-\infty}^{\infty} P(x)x^2\,dx - \overline{x}^2 = \frac{\pi^2}{6\beta^2}, \quad (5)$$

where C is the Euler–Mascheroni constant appearing through the integration. From $\partial P(x)/\partial x = 0$, we can also easily get the following modal value of the MFT distribution:

$$\overline{x}_{\text{mod}} = \ln\alpha/\beta. \quad (6)$$

Estimators for the parameters of the distribution (2) can be derived from the maximum likelihood method (see appendix A), which implies a system of equations to be resolved numerically through the iterative procedure as follows:

$$\frac{n}{\alpha} = \sum_{i=1}^{n} \exp(-\beta x_i) \quad \text{and}$$

$$\frac{n}{-\beta} + \sum_{i=1}^{n} x_i = \alpha \sum_{i=1}^{n} x_i \exp(-\beta x_i). \quad (7)$$

Numerical solution of (7) provides us with the parameter estimators. Technically, to avoid floating overflow when resolving (7), the actual values of sensible and latent fluxes in watts per square meter can be scaled by, for example, 10^3, which should be coordinated with the actual number of observations used for estimation. Estimation of the local monthly mean in a 2° box can involve from 5 to several thousand samples per month in poorly and well-sampled areas, respectively (Gulev et al. 2007a). Scaling of surface fluxes with, for example, 10^3 returns the values of β multiplied by 10^3. Below we discuss surface fluxes in units of watts per meter squared and values of β in 10^{-3} meters squared per watt.

Figure 2 shows the evolution of the MFT PDF (2) with the parameters α and β. The scale parameter, which holds the dimension of 10^{-3} meters squared per watt, is inversely proportional to the standard deviation of surface flux (5). It controls the squeeze of the MFT distribution, implying a gentle distribution under smaller β and more peaked distribution under larger β. Nondimensional α under fixed β determines the modal value. If $\alpha < 1$, then modal values will be negative with zero modal value achieved under $\alpha = 1$. Figure 1 also shows approximations of the empirical histograms of sensible and latent heat fluxes for different regions by the MFT distribution. This distribution fits well to the data in most locations for both sensible and latent fluxes. The Kolmogorov–Smirnov (K–S) test (e.g., D'Agostino and Stephens 1986) returns the probability that the goodness of fit of distribution (2) is higher than 95% for most cases considered. We also applied more powerful tests of goodness of fit (Littell et al. 1979; Coles 1989) based on order statistics (Michael 1983) and giving more weights to the tails than the K–S test. These alternative tests give similar results, implying that MFT fits well with the data in most cases. Some further information on testing goodness of fit will be given in section 4. However, besides the goodness of fit, estimating the differences in the MFT distribution parameters one should also consider the confidence intervals for α and β. We will address this issue in section 6 using the formalism presented in appendix A.

A reasonable question may arise about whether the selected MFT PDF is the most appropriate for the distribution of surface turbulent fluxes. We investigated the applicability of a number of alternative distributions, such as the three-parametric Weibull distribution and the Fréchet distribution, to our task. A simple application of K–S (or any alternative tests) for justifying the choice of MFT would not suffice because it does not necessarily exclude the applicability of the alternative distributions (type 2 error). To test the competitive applicability of the alternative distributions, we have used here the Neyman–Pearson criterion (see appendix A). Results of the comparative assessment are presented in section 4.

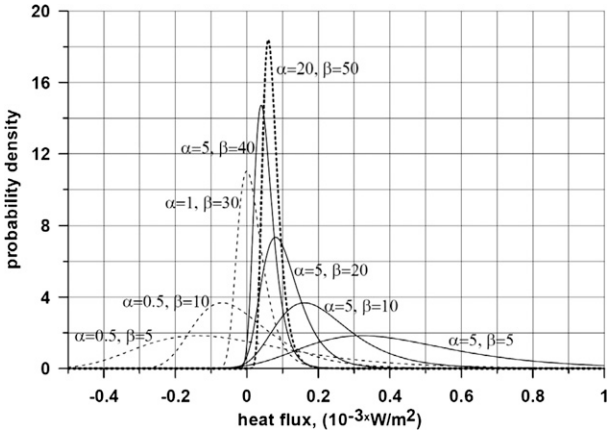

FIG. 2. PDFs of the MFT distribution for different location (α) and scale (β) parameters.

3. Data and preprocessing

For further analysis of the probability distribution characteristics of surface turbulent heat fluxes over the World Ocean, we used 6-hourly state variables [10-m scalar wind speed, sea surface temperature (SST), 2-m air temperature and humidity, sea level pressure (SLP)] from the NCEP–NCAR reanalysis (Kalnay et al. 1996; Kistler et al. 2001) for the 61-yr period from 1948 to 2008. Original 1.875° × ≈1.9° resolution (Gaussian grid) data were interpolated onto a 2° × 2° grid by the method of local procedures (Akima 1970) also used in Gulev et al. (2007a,b). The NCEP–NCAR reanalysis provides turbulent fluxes as diagnosed by the operational model as diagnostic variables representing 6-hourly averages starting at the reference time. To provide comparability with the VOS data, we recomputed the fluxes from 6-hourly reanalysis state variables, keeping in mind that the state variables represent 6-hourly forecasts from the reference time. Sensible and latent heat fluxes from reanalysis state variables were estimated by the COARE 3.0 algorithm (Fairall et al. 2003), which is considered to be the least biased among the available surface flux schemes (Brunke et al. 2003). The NCEP–NCAR air temperature and humidity (given at 2-m height) were adjusted to 10-m height, and the surface wind speed (reported at 10 m) was adjusted to neutral stability using the flux-profile relationships from Fairall et al. (2003). This is exactly the same procedure that has been applied for the flux computations in Gulev et al. (2007a,b).

For the simulation of sampling density implied by VOS, we also used the recent update of ICOADS marine reports for the period 1948–2007 (Woodruff et al. 2011). This archive includes data from different types of platforms (merchant and research vessels, moored and drifting buoys, etc.). A detailed description of the present state of the ICOADS collection is given by Worley et al. (2005) and Woodruff et al. (2011). Details of data coverage for different variables in space and time can be found in Gulev et al. (2007a,b). As in Gulev et al. (2007a), in this study we have only used the reports containing the whole set of parameters needed for flux computations (SST, air temperature, SLP, humidity, and surface wind). Gulev et al. (2007a) provided estimates of sampling uncertainties for radiation fluxes and thus also required the presence of cloudiness in the reports. However, the sampling density of cloudiness is quite similar to that of the other variables (see, e.g., Bedacht et al. 2007), and in practice the number of reports used in this study was just 2% higher compared to that employed by Gulev et al. (2007a).

After recomputing the individual 6-hourly turbulent heat fluxes, two datasets were formed. The first dataset consisted of the recomputed fluxes, which have regular sampling (i.e., 120 reports per a 30-day month). Another dataset was produced by the procedure of subsampling aimed to simulate the VOS sampling density. This procedure was described in detail in Gulev et al. (2003, 2007a) and provided the matching of the computed 6-hourly fluxes to the dates and UTC hours of the ICOADS reports.

For the regularly sampled and subsampled flux datasets, we computed characteristics of the MFT distribution for every calendar month. Monthly values of the location and scale parameters (α_h, β_h and α_e, β_e for sensible and latent heat fluxes, respectively) as well as monthly means, intra-monthly standard deviations, and modal values were computed according to (5)–(7) using the iterative algorithm. Furthermore, we estimated different percentiles of turbulent sensible and latent heat fluxes, including fluxes of rare occurrences corresponding to, for example, 99.9th and 99.99th percentiles.

All characteristics of the statistical distributions were computed for 2° × 2° grid cells to obtain spatial fields. For the statistics derived from the subsampled fluxes, this procedure of averaging still leaves gaps in the fully unsampled 2° × 2° boxes. Gap filling using different interpolation methods results in yet another source of uncertainties in spatial fields (Kent et al. 2000; Sterl 2001, 2004; Gulev et al. 2007a). To produce fields of flux statistics on a regular grid, we used the Akima (1970) method of local procedures. Characteristics of the method, including resulting uncertainties, are given in Gulev et al. (2007a).

According to Gulev et al. (2007a), the comparison of the monthly means derived from the regularly sampled and subsampled fluxes allows for the estimation of sampling uncertainties in surface flux fields. Thus, the squared difference between the monthly means of the regularly sampled variables or fluxes (x_o) and the VOS-like sampled variables (x_u) gives the squared *total sampling uncertainty,* χ^2, as follows:

$$\chi^2 = (x_o - x_u)^2. \tag{8}$$

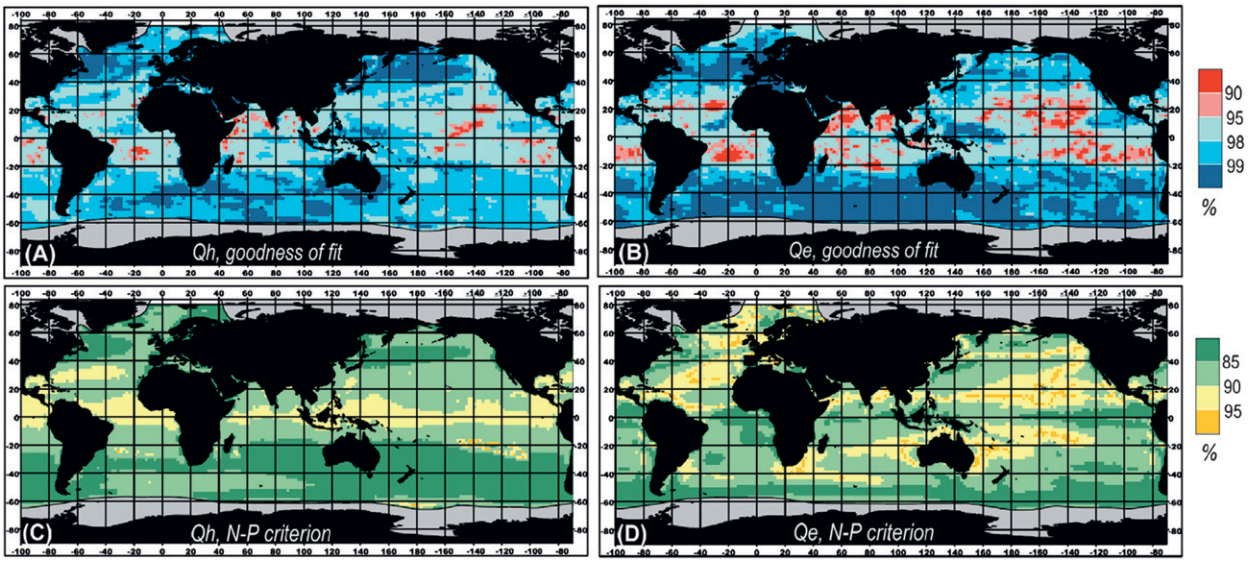

FIG. 3. (top) Spatial distribution of the goodness of fit of the MFT distribution (%) estimated with the K–S test for (a) sensible and (b) latent heat fluxes. Pink and red areas indicate where the goodness of fit drops below 95% and 90%, respectively. (bottom) Significance levels, estimated according to the Neyman–Pearson criterion, at which both the MFT and 3-parameter Weibull distribution can be applied for the description of surface (c) sensible and (d) latent fluxes. Light and dark yellow areas indicate where the effectiveness of the Weibull distribution is competitive to MFT at the 90% and 95% significance levels, respectively.

Similarly, differences were computed for the distribution parameters (location, scale, means, modal values, percentiles), derived from the regularly sampled and subsampled data.

4. Climatology of characteristics of statistical distribution of surface turbulent fluxes

Prior to the analysis of climatologies of the distribution parameters and derived extreme surface fluxes, we need to address the issue of goodness of fit of the MFT distribution and the competitive applicability of alternative distributions for the description of turbulent heat fluxes. In Figs. 3a,b, we show the goodness of fit of the MFT distribution estimated according to the K–S test. For the sensible flux, it drops below 95% only in few locations in the South Atlantic tropics, the western equatorial Indian Ocean, and the western equatorial Pacific. For Q_e, regions of potentially poor fit of the MFT distribution are generally collocated with those of Q_h, but are somewhat larger, especially in the North Pacific tropics. Application of the alternative Michael's test (Littell et al. 1979; Coles 1989) results in a minor enlargement of the areas with poor fit for Q_h, leaving the corresponding areas for Q_h almost unchangeable. Figures 3a,b indicate areas where the results based on MFT distribution should be considered with caution. These areas are quite persistent throughout the year, with some minor enlargement during the summer season.

Besides the goodness of fit, we also analyzed the applicability of the alternative distributions (Weibull and Fréchet distributions). For this purpose we adopted the Neyman–Pearson criterion for testing the hypothesis that an alternative distribution fits better to the data than the MFT distribution. According to the formalism presented in appendix B, we have estimated the statistics L as follows:

$$L = \ln\frac{p_{\mathrm{alt}}}{p_{\mathrm{MFT}}}, \tag{9}$$

where p_{alt} is the competitive distribution (e.g., Weibull or Fréchet distribution) and p_{MFT} is the suggested MFT distribution. Then, analyzing this statistics at a given significance level, we either accepted or rejected the null hypothesis that the surface turbulent fluxes are distributed according to MFT PDF. Details of the computation of L are given in appendix B. Figures 3c,d show the significance levels at which both MFT and the three-parameter Weibull distribution can be applied to the description of surface turbulent fluxes. For both sensible and latent fluxes, there are only a few locations where the Weibull distribution is as effective as MFT at the 95% level. In the case of sensible heat flux, areas characterized by the competitive effectiveness of both distributions are associated with the tropics. For the latent heat in the Northern Hemisphere, these areas are located in the eastern parts of the midlatitudinal and subtropical oceans. The lowest probability of the effectiveness of the Weibull distribution is associated

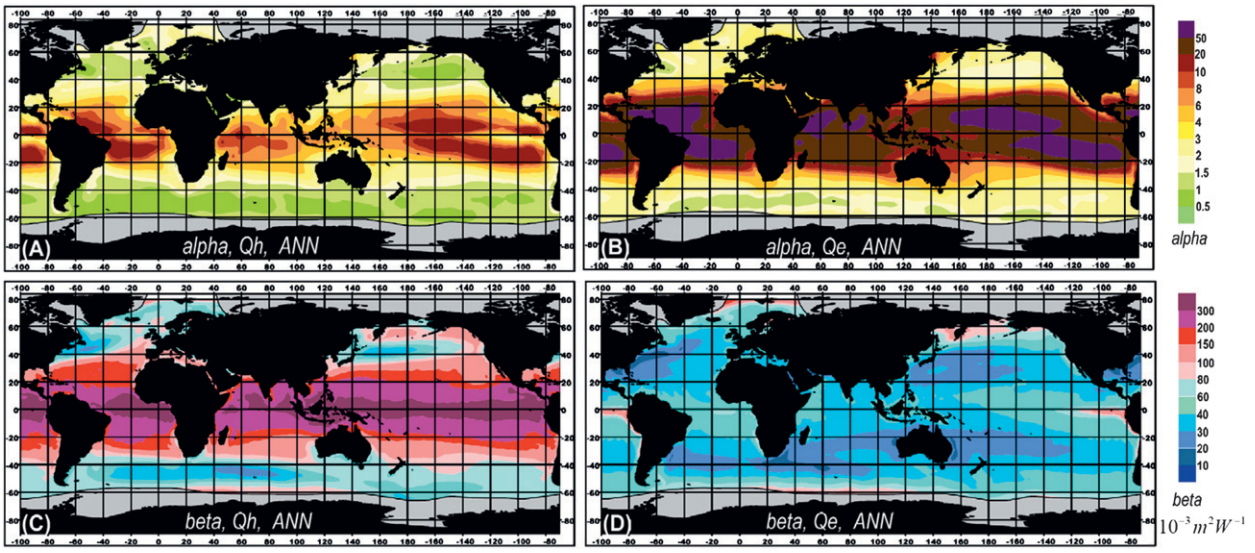

FIG. 4. Annual mean climatologies of the (top) location and (bottom) scale parameters of the MFT distribution for (a),(c) sensible and (b),(d) latent heat fluxes.

with the western boundary current regions of the Northern Hemisphere. Remarkably, in many cases, the areas where both distributions are competitive are closely associated with the regions where the goodness of fit for MFT falls below 95%. Similar estimations performed for the Fréchet distribution (no figure shown) demonstrate that this distribution is less competitive with MFT compared to the three-parameter Weibull distribution.

Figure 4 shows the spatial climatological distributions of the location and scale parameters of the MFT distribution for sensible and latent heat fluxes for the period 1948–2008. The smallest values of α_h of less than 1 (fluxes are negative, i.e., directed from the atmosphere to the ocean) are observed in the Southern Ocean, in the northwest Atlantic, and central North Pacific. The highest values of α_h of 10–20 are observed in the tropics. In the regions of high sensible fluxes (Labrador Sea and western boundary currents), α_h ranges from 2 to 3. For the latent heat flux (Fig. 3b), the location parameter α_e is generally 1.5–3 times higher than α_h and ranges from a minimum of 1–2 (in the Southern Ocean and in the Northern Hemisphere mid- and subpolar latitudes) to 30–50 in the tropics. In the boundary current regions, the values of α_e show local maxima of 4–6. The smallest values of β_h (10–15 $\times$ 10^{-3} m^2 W^{-1}) are in the areas where mean fluxes and their synoptic standard deviations are locally high (Labrador Sea, Gulf Stream, and Kuroshio). The largest values of β_h (200–300 $\times$ 10^{-3} m^2 W^{-1}) are observed in the eastern tropics of the Atlantic and Pacific, where short-period synoptic variability of fluxes is small (Fig. 3c). For the latent heat flux, β_e varies from 5–10 $\times$ 10^{-3} m^2 W^{-1} in the midlatitude areas of locally high short-period variability of evaporation to more than 100 $\times$ 10^{-3} m^2 W^{-1} in the eastern equatorial Pacific and in the northern and southern subpolar latitudes, where synoptic variability of Q_e is quite small. Analysis of the seasonal variability in the parameters of MFT distribution (no figure shown) implies that the largest magnitudes of the annual cycle are found in the Northern Hemisphere midlatitudes where seasonal changes in the scale parameter amount to 60%–100% and are somewhat larger for Q_h than for Q_e. This is in agreement with the strong seasonal cycle in the magnitudes of synoptic variability of turbulent fluxes (and, thus, their standard deviations steering β) in the midlatitudes and subtropics.

For reference, Fig. 5 shows the global climatological maps of sensible and latent heat fluxes for January and July. Flux values were derived from the parameters of MFT distribution α and β according to (5) for individual calendar months, and then they were averaged to obtain climatological fields. Turbulent fluxes in Fig. 5 are qualitatively consistent with the other climatologies (e.g., Josey et al. 1999; Yu and Weller 2007). Local maxima of Q_h during the boreal winter are observed in the Labrador Sea (>200 W m^{-2}) as well as in the Gulf Stream and Kuroshio (about 120 and 160 W m^{-2}, respectively). The largest values of Q_e in the Gulf Stream and Kuroshio amount to 300 W m^{-2} being somewhat larger than those in the Indian Ocean tropics and in the Agulhas Current (150–200 W m^{-2}). A direct comparison of climatological flux fields with Josey et al. (1999), Yu and Weller (2007), or Large and Yeager (2009), for example, is difficult since different data and methods were used and different periods were considered. For the period of 1981–2005, the

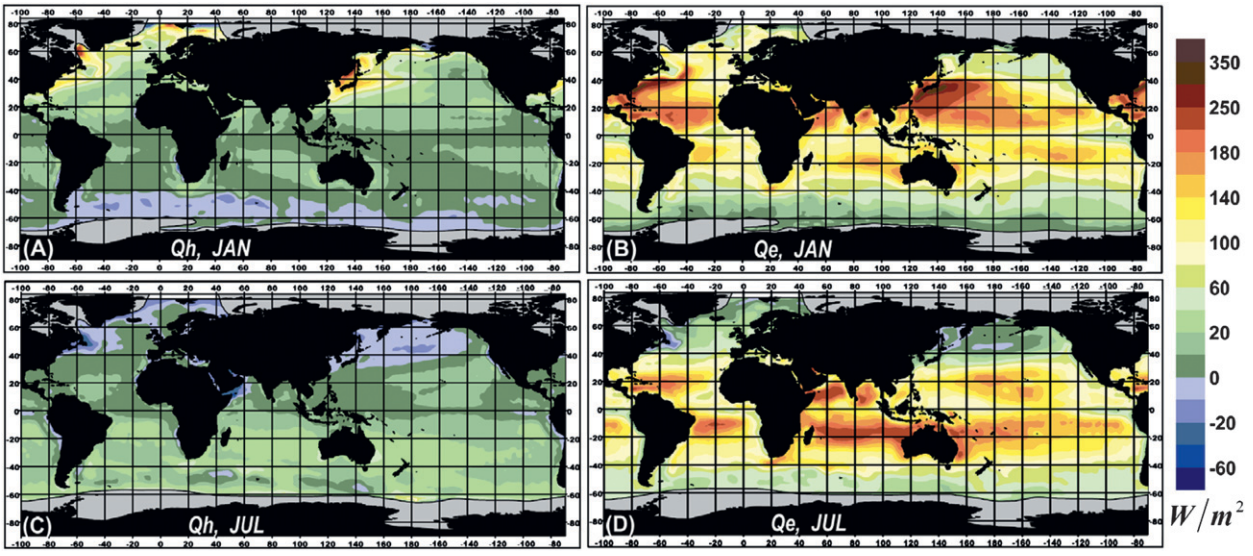

FIG. 5. Global climatological maps of (a),(c) sensible and (b),(d) latent heat fluxes for (top) January and (bottom) July, derived from the parameters of the MFT distribution.

climatological fluxes in Fig. 5 are slightly higher compared to those of Yu and Weller (2007), with the largest differences of 5–15 W m^{-2} for the sensible flux and 10–15 W m^{-2} for the latent flux. Also, the localization of subpolar areas of relatively small negative latent fluxes (net release of latent energy back into the air) during the warm season is in agreement with Yu and Weller (2007). However, here the climatological fluxes are shown for reference only since we are focused on the estimation of the flux distribution characteristics, including extreme fluxes, rather than on the development of a new surface flux climatology.

Turbulent heat fluxes (Fig. 5) and MFT distribution parameters (Fig. 4) can be jointly considered using a two-dimensional α–β diagram, presented in Fig. 6 and showing mean values of turbulent fluxes (5) in the coordinates of the location and scale parameters. This diagram shows that the variations in the range of relatively small fluxes are primarily driven by the location parameter, while changes in the range of high flux values (whose contours are almost parallel to the α axis) are steered by the scale parameter. In Fig. 6 we show the different points characterized by exactly the same sensible and latent monthly-mean fluxes for January 1996 [climatological values are not applicable here because of the nonlinearity of (5)]. Unsurprisingly, the same monthly-mean fluxes can be observed under very different α and β. Mean monthly Q_e = 150 W m^{-2} in the Atlantic tropics is characterized by α typically exceeding 20 and β lying from 20 to 30 $\times$ 10^{-3} m^2 W^{-1}. The same monthly mean in the boundary current regions (where surface fluxes are highly variable) is characterized by much smaller values of the parameters and quite a different shape of distribution. More extended characteristics of the MFT distribution are demonstrated in Figs. 6b,c, showing modal values (Fig. 6b) and 99th percentiles of turbulent heat fluxes (Fig. 6c) overplotted with each other in the background. Smaller α and β imply a stronger asymmetry of the distribution and a larger deviation of the mean from the modal value. The largest extreme fluxes are observed under relatively small β (implying high standard deviations) in a wide range of α. For instance, p_{99} of 2000 W m^{-2} can be achieved under β not exceeding 3–5 $\times$ 10^{-3} m^2 W^{-1}, which can be observed in the Gulf Stream and Kuroshio regions for Q_e (with α_h ranging from 5 to 10) and in the Labrador Sea for Q_h (with α_e being around 2–3). At the same time in the tropical Atlantic also characterized by strong winter latent heat fluxes (Fig. 6a), the expected extreme fluxes are several times smaller—around 300 W m^{-2}. Because of differences in the shape of distribution, the mean monthly latent heat flux of 150 W m^{-2} implies the 99th percentile of about 330 W m^{-2} in the tropics and more than 700 W m^{-2} in the Gulf Stream.

In Fig. 7 we show the two-dimensional occurrence distributions of the monthly-mean surface sensible and latent fluxes over the global ocean in the coordinates of α and β. They were computed from 2° $\times$ 2° monthly values of Q_h, Q_e, α, and β were scaled with cosφ, φ being latitude. In other words, counts in Fig. 7 represent the fraction of the ocean area characterized by sensible and latent fluxes steered by given α and β parameters of the MFT distribution. Initially, these diagrams were computed for individual months from January 1948 to December 2008 and then were averaged over a 61-yr period for each α–β

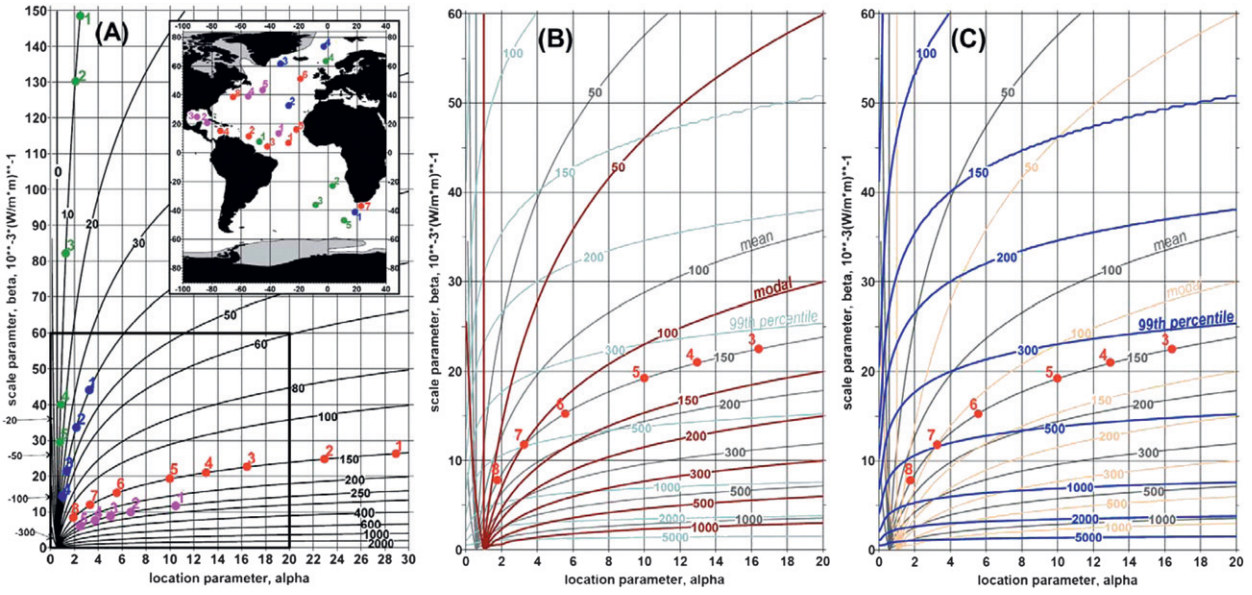

FIG. 6. (a) Mean values of turbulent fluxes (5) in the coordinates of the location and scale parameters. Inlay map shows the points characterized by the same mean January 1996 fluxes: 250 W m^{-2} latent flux (magenta), 150 W m^{-2} latent flux (red), 40 W m^{-2} sensible flux (blue), and 10 W m^{-2} sensible flux (green). (b) Contours of modal values of surface turbulent heat fluxes (thick brown) overplotted with mean values (light gray) and the 99th percentile (light blue) in the coordinates of the location and scale parameters for the range of parameters bounded by the boldface rectangle in (a). (c) Contours of the 99th percentile of surface turbulent heat fluxes (thick blue) overplotted with mean (light gray) and modal (light brown) values in the coordinates of the location and scale parameters for the range of parameters bounded by the boldface rectangle in (a). Red points in (b) and (c) recall the corresponding points from (a) from 3 to 8, for which mean latent heat flux equals 150 W m^{-2}.

class. Two-dimensional distributions for Q_h and Q_e are remarkably different. For sensible heat flux, the highest occurrence is concentrated in the range of $0.1 < \alpha < 2.0$ and spans over β ranging from 10–15 $\times$ 10^{-3} to about 100 $\times$ 10^{-3} m^2 W^{-1}. For latent heat flux, the maximum occurrence is observed under α ranging from 1 to 10–20 and β lying in the range from 10 to 30 $\times$ 10^{-3} m^2 W^{-1}, corresponding to the tropical and midlatitudinal regions. Distribution of Q_h is largely dominated by the scale parameter, while distribution of Q_e is steered by the location parameter under moderate β and by the scale parameter under smaller α.

Statistical distributions of turbulent fluxes allow for the estimation of extreme flux values. Figure 8 shows climatological January and July 99th percentiles of sensible and latent heat fluxes over the global ocean. These estimates were derived from the CDF of the MFT distribution (4) fitted to the fluxes for individual months. The largest January 99th percentiles of turbulent fluxes (Fig. 8) amount to 1000–1200 W m^{-2} in the Gulf Stream and Kuroshio regions for the latent heat flux and in the Labrador and Japan Seas for the sensible heat flux. In July (Figs. 8b,d) the largest extremes are observed in the subpolar Southern Ocean for Q_h (up to 350–400 W m^{-2}) and in the Southern Hemisphere subtropics and midlatitudes for Q_e, with the local maxima of more than 600 W m^{-2} in the East Australian Current system. Extreme fluxes for individual years can be considerably higher compared to the climatologically averaged 99th percentiles. Figures 8e,f show the maxima of the 99th percentiles of turbulent sensible and latent heat fluxes observed during the 61-yr period. These maxima amount to more than 1500 W m^{-2} during boreal winter in the Northern Hemisphere and during austral winter in the Southern Hemisphere. The strongest absolute extremes of sensible and latent heat fluxes are observed in the subpolar latitudes for Q_h and over the western boundary current regions and subtropics for Q_e. Locally high values of more than 1000 W m^{-2} are also identified in the Red Sea, Persian Gulf, and in the Arabian Sea. Note, however, that estimates for the Arabian Sea should be taken with caution because MFT distribution here may not always fit satisfactorily with the data (Figs. 3a,b). The zonally averaged different percentiles of latent and sensible heat fluxes for January and July are shown in Fig. 9. During the Northern Hemisphere, winter zonal extremes of Q_e amount to 480 and 850 W m^{-2} for 99th and 99.99th percentiles, respectively, in the subtropics. The corresponding extreme values of Q_h in the mid- and subpolar latitudes are equal to 300 and 560 W m^{-2}. During austral winter extreme sensible and latent fluxes in the Southern Hemisphere are typically 20%–30% smaller compared to those for the boreal

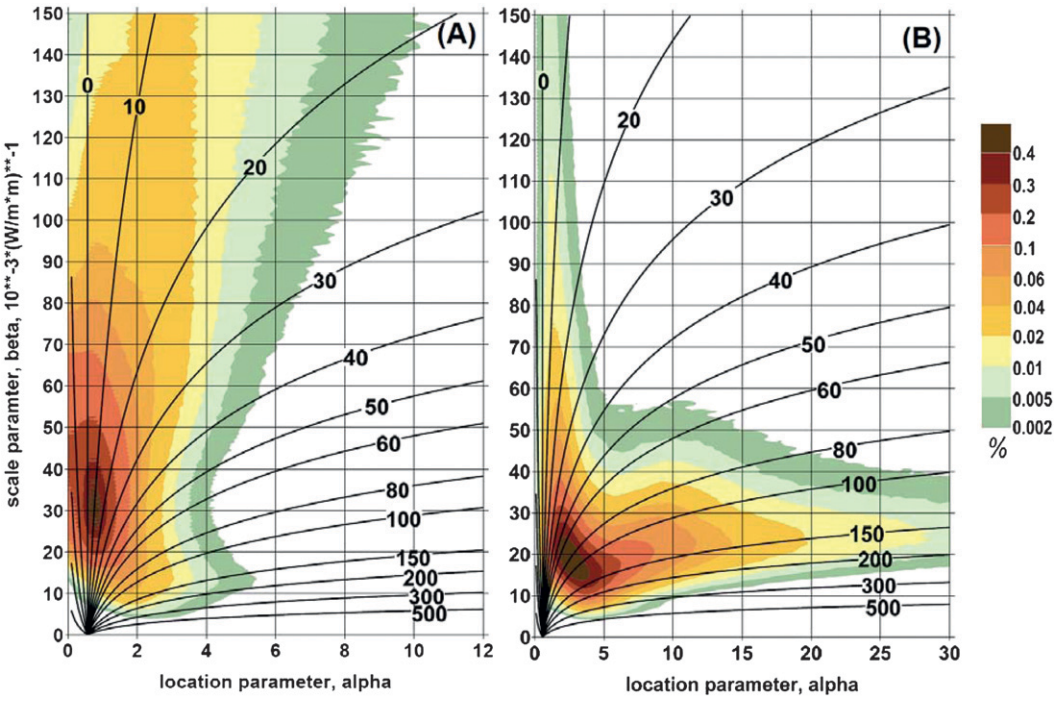

FIG. 7. Two-dimensional occurrence distributions of the monthly-mean surface (a) sensible and (b) latent turbulent heat fluxes over the global ocean in the coordinates of the location and scale parameters of the MFT distribution. Black contours correspond to the mean fluxes as in Fig. 6.

winter in the Northern Hemisphere. Figure 9 also clearly shows strong change in the squeeze of the MFT distribution from winter to summer, in agreement with the seasonal changes in the parameters of distribution.

5. Interannual variability in the characteristics of statistical distributions of surface turbulent fluxes

Now let us consider the interannual variability of surface turbulent fluxes in the context of the parameters of MFT distribution. Figure 10, on the α–β diagram, schematically shows some changes in the 99th percentile of turbulent fluxes, which are, hypothetically, caused by the change in the mean flux by 20 W m^{-2} under different associated changes in α and β. The value of 20 W m^{-2} gives a typical range of interannual variations of surface fluxes and also represents a reasonable estimate of the linear trends during the recent decades (e.g., Yu and Weller 2007; Yu 2007; Gulev et al. 2007b). According to Fig. 10, a positive change in the mean turbulent flux can be associated with both positive and negative tendencies in extreme fluxes and can vary from a few watts per square meter to several hundred watts per square meter, depending on the changes in α and β. Similarly, the decrease of the mean turbulent flux by 20 W m^{-2} under different tendencies in α and β may result in the change of the 99th percentile from -150 W m^{-2} to more than 100 W m^{-2}.

Keeping this in mind, we show in Fig. 11 the linear trends (1948–2008) in the means and 99th percentiles of sensible and latent heat fluxes for the periods from October to March and from April to September corresponding to the cold (warm) and warm (cold) seasons in the Northern (Southern) Hemispheres. In the Southern Hemisphere, NCEP–NCAR state variables are influenced by the temporal inhomogeneity of data assimilation input (e.g., White 2000; Sterl 2004). However, here we are not making new inferences about secular changes in the fluxes computed from reanalyses, but rather quantifying the differences between the changes in mean and extreme fluxes. Details of the estimation of the trend significance are explained in Fig. 11. Figures 11a–d show statistically significant upward trends in turbulent fluxes in the western boundary current regions (4–7 W m^{-2} decade^{-1} for Q_e and 2–3 W m^{-2} decade^{-1} for Q_h). Seasonality of the trend patterns is clearly evident for the eastern Atlantic tropics, Kuroshio region, Bengal Bay, and South China Sea, where cold and warm seasons are characterized by significantly positive and negative trends, respectively. These changes in the trend sign are likely to be imposed by the change in the summer monsoon breaks reported, for example, for the Indian Ocean by Ramesh Kumar et al. (2005, 2009). Linear trends for 1981–2005 (no figure

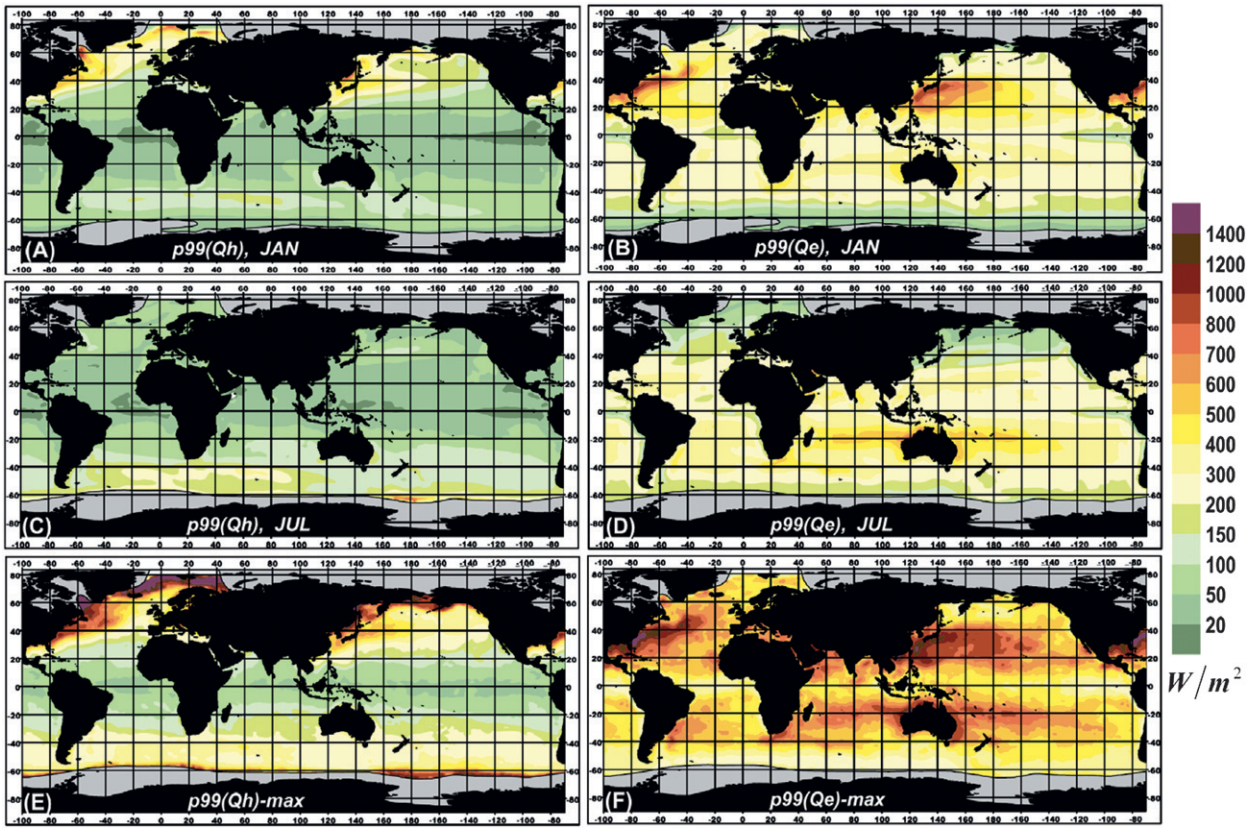

FIG. 8. Climatological (top) January and (middle) July 99th percentiles of (a),(c) sensible and (b),(d) latent heat fluxes over the global ocean, and the maxima of the 99th percentiles of turbulent (e) sensible and (f) latent heat fluxes observed during the 61-yr period.

shown) are very consistent with Yu and Weller (2007) estimates performed for this period using OA WHOI daily fluxes. Similarly, our estimates of trends in the latent heat flux for the decades of 1970s and 1990s are in agreement with the interdecadal changes in evaporation reported by Yu (2007).

In the regions where linear trends in extreme turbulent fluxes (Figs. 11e–h) are qualitatively consistent with those for the mean fluxes, they typically show stronger tendencies that amount to more than 15 W m^{-2} $decade^{-1}$ for Q_e and up to 10 W m^{-2} $decade^{-1}$ for Q_h in the western boundary current regions. However, there are areas where tendencies in the mean and extreme fluxes disagree. First of all in the Southern Ocean between 20°W and 120°E, negative trends in the mean fluxes imply positive trends in extreme fluxes for both Q_h and Q_e. For the period April–September in the Kuroshio region, mean Q_h exhibits slightly negative trends, while trends in extreme fluxes are significantly positive. Analysis of trends for individual months (no figure shown) also shows differences in the trend sign for Q_e in the subpolar and eastern subtropical Atlantic in boreal winter and for Q_h in the Agulhas Current in austral winter.

It is interesting to consider trends in the mean and extreme fluxes with respect to the tendencies in the parameters of MFT distribution (Fig. 12). In the western boundary current regions (Gulf Stream, Kuroshio, Agulhas), positive trends in Q_e are associated with slightly growing α and the negative change in β. Negative trends in Q_e in the Northern Hemisphere midlatitudes are associated with a slightly negative change in α and increasing β. Negative trends in Q_e in the tropical Pacific are associated with the strong negative changes in α and the weakly growing β. Positive Q_e trends during April–September in the central Indian Ocean are implied by the negative change in both α and β. We considered the following ratios between the trend magnitudes in extreme and mean fluxes:

$$\xi(Q_e) = \frac{\partial p_{99}(Q_e)}{\partial Q_e} \quad \text{and} \quad \xi(Q_h) = \frac{\partial p_{99}(Q_h)}{\partial Q_h}, \quad (10)$$

shown in Figs. 12e,f for the latent heat flux. In the Northern Hemisphere midlatitudes and in the central Indian Ocean, ratios (10) typically exceed 2–3, implying a relatively strong change of extreme fluxes for a given tendency in the mean fluxes. The largest ξ values (up to 10–15) are observed in

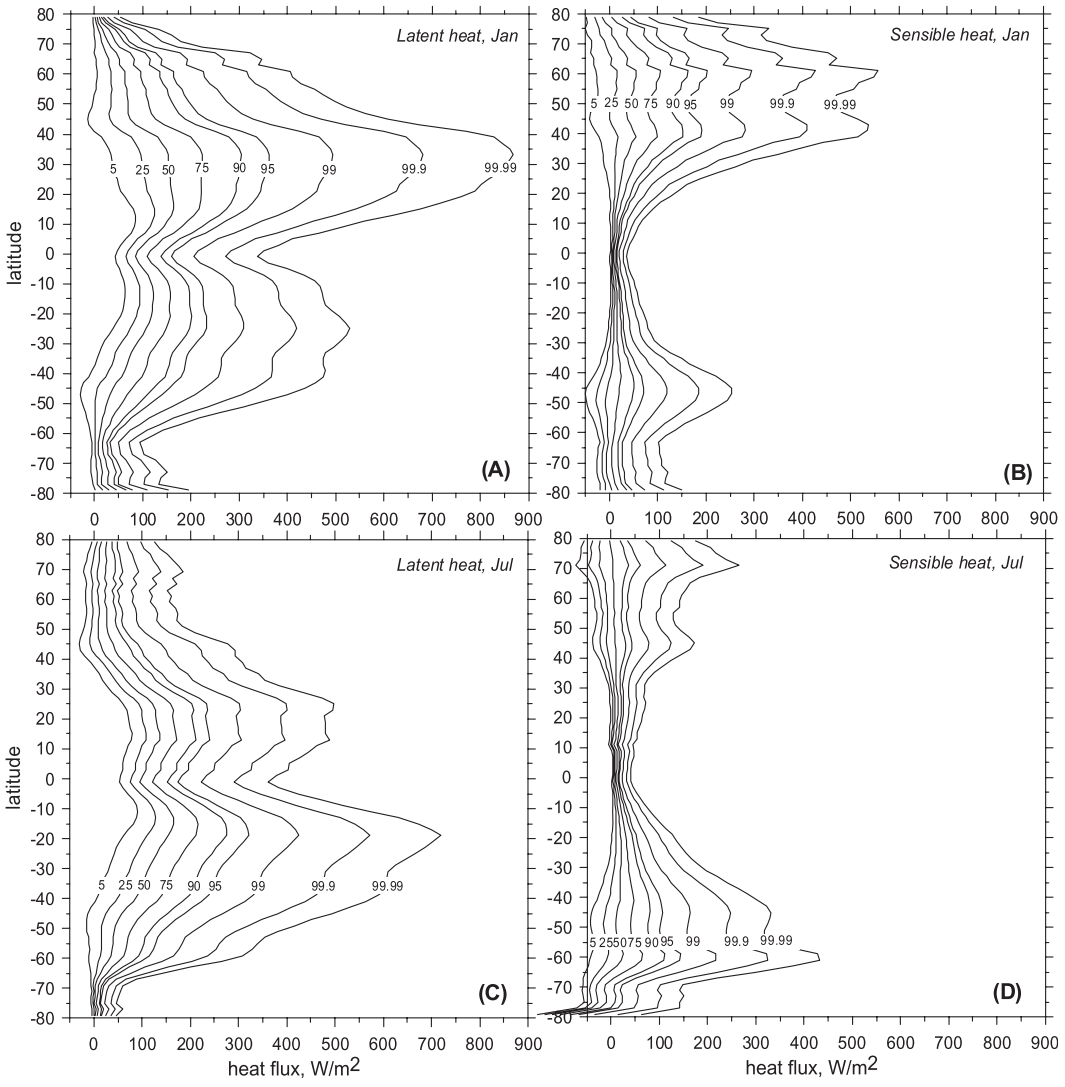

FIG. 9. Zonally averaged different percentiles of the (a),(c) latent and (b),(d) sensible heat fluxes for (top) January and (bottom) July.

the western boundary current regions, where strongly decreasing β (and, thus, the magnitude of the synoptic variability of fluxes) implies a strong growth of extreme fluxes (see diagram in Fig. 10). In the Pacific and Atlantic tropics, values of ξ vary from -1 to 2, implying either a smaller magnitude of trends in p_{99} compared to the mean fluxes or even opposite tendencies in the mean and extreme fluxes. This effect is also clearly visible in the Southern Ocean between 20°W and 120°E in both cold and warm periods. The same analysis performed for Q_h (not shown) reveals qualitatively similar results with, however, stronger spatial variability of the ratio (10). Sensible fluxes are generally smaller in magnitude and are characterized by smaller α and larger β compared to the latent fluxes (Figs. 4, 6). This implies a potentially large scatter of tendencies in extreme values associated with given changes in the mean values.

Now it is interesting to consider the variability in turbulent fluxes and associated variations in the MFT distribution parameters and extreme fluxes at interannual time scales. During boreal winter (JFM), the highest interannual standard deviations of Q_e in excess of 30–40 W m^{-2} are observed in the Gulf Stream and Kuroshio. The strongest values of $\sigma(Q_e)$ during June–September (JAS) (30–35 W m^{-2}) are observed in the tropics. In the areas of the strongest $\sigma(Q_e)$ in the western boundary current regions, standard deviations of α (no figure shown) amount to 10%–15% of the mean values, with $\sigma(\beta)$ being from 5% to 10% of the mean values. At the same time, tropical maxima of $\sigma(Q_e)$ are associated with the magnitudes of $\sigma(\alpha)$ of up to 80% of the mean values. Figure 13 shows the ratio between interannual standard deviations of the mean fluxes and their 99th percentiles for Q_h (Figs. 13a,c) and

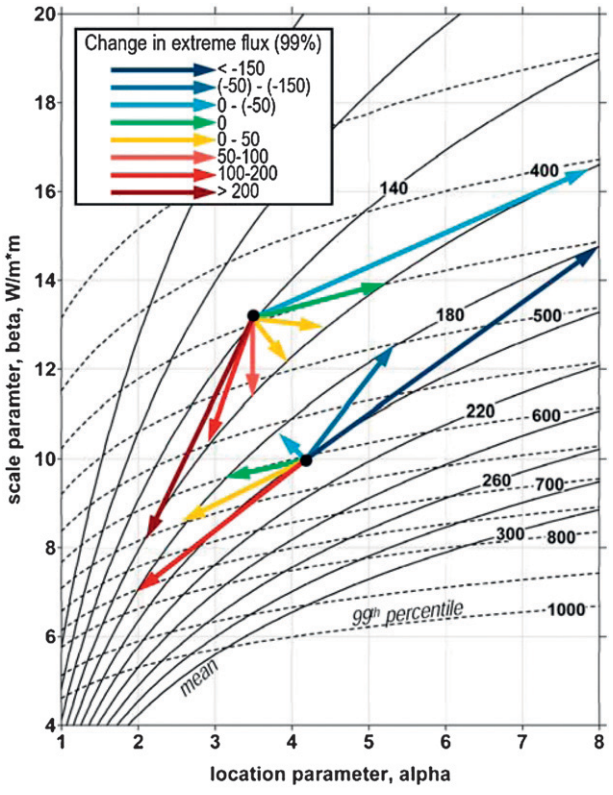

FIG. 10. Hypothetical scheme, showing potential changes in the 99th percentile of turbulent fluxes, which are implied by the change is the mean flux by 20 W m^{-2} under different associated changes in α and β. Upper fantail of the arrows corresponds to the positive change of the mean flux by 20 W m^{-2} and the lower fantail to the negative. Colors of the arrows show the sign and the magnitude (W m^{-2}) of the associated changes in the 99th percentile of surface fluxes under different tendencies in α and β.

Q_e (Figs. 13b,d) for JFM and JAS. In the subpolar latitudes during the warm season, extreme fluxes exhibit much stronger interannual variability compared to the mean fluxes. Indeed, strong cyclones (and associated extreme fluxes) can occur here even in summer, although they do not significantly affect seasonal means. In the tropics the magnitude of interannual variability of extreme fluxes only slightly exceeds the magnitude of variability in the means, and sometimes it is even slightly smaller (for Q_h). This is different from the ratio between the magnitudes of linear trends (Fig. 12), which shows quite high values in the Indian Ocean tropics. Figures 13e–h show the maps of correlation between mean and extreme fluxes on interannual time scales. Time series of the anomalies were detrended for the computation of correlation coefficients. Over nearly half of the global ocean correlations are less than 0.7, implying that less than 50% of the variability in means is accounted for by the variability in extreme fluxes. Furthermore, in many areas (subpolar regions for Q_h and tropical areas for Q_e), the correlation drops below the level of significance, implying that changes in extreme and mean fluxes are not coordinated. Thus, mean and extreme fluxes regionally exhibit not only significantly different linear trends but also quite different interannual variability.

6. Impact of sampling on characteristics of statistical distribution of surface fluxes

Analysis of probability distributions of surface turbulent fluxes is also useful for the estimation of the impact of sampling on climatological surface fluxes. This estimation was provided for the period 1948–2007 for which VOS data were available from ICOADS. Figures 14a,b show the total sampling error (8) normalized by the mean surface flux magnitudes. In the Southern Ocean for both Q_h and Q_e, the total sampling uncertainty (30–50 W m^{-2}) closely matches or even exceeds 100% of the mean flux values. Winter values of the total sampling error may amount to 60–70 W m^{-2} (Gulev et al. 2007a) for both Q_h and Q_e in the Labrador Sea and the Southern Ocean. Using MFT distribution, we can extend the analysis of sampling uncertainties to the estimation of the impact of sampling on extreme fluxes. These estimates were derived by the method described in section 3. Figures 14c,d show the climatological total sampling error in the 99th percentile of the sensible and latent heat fluxes. Uncertainties in 99th percentiles are typically 2–3 times higher than those in the mean fluxes, the largest occurring in the mid- and subpolar latitudes of both hemispheres (up to 100 W m^{-2} for climatological values). In winter (no figure shown), the total sampling uncertainty in extreme fluxes may locally amount to 200–300 W m^{-2} for p_{99}, being considerably larger for the higher percentiles. Note that sampling errors in extreme fluxes as well as in α and β were only estimated in the areas where at least five VOS observations per month were available for at least 10 yr in the record. This limitation leaves blanked the poorly sampled areas in the Southern Ocean in Figs. 14c–j. For some of these cells, however, the total sampling error in the mean could be estimated (Figs. 14a,b) because the requirements for its estimation are less restrictive than those for the computation of PDF from the subsampled time series (Gulev et al. 2007a).

Figures 14e,f show climatological maps of the following ratio between the relative total sampling errors in the extreme and mean fluxes:

$$\mu_{99}(Q) = \frac{\chi[p_{99}(Q)]/p_{99}(Q)}{\chi(Q)/Q}. \qquad (11)$$

Remarkably, the spatial distribution of the ratio μ is largely dominated by the location parameter α, (cf. with Fig. 4), being <1 in the subpolar and midlatitudes and

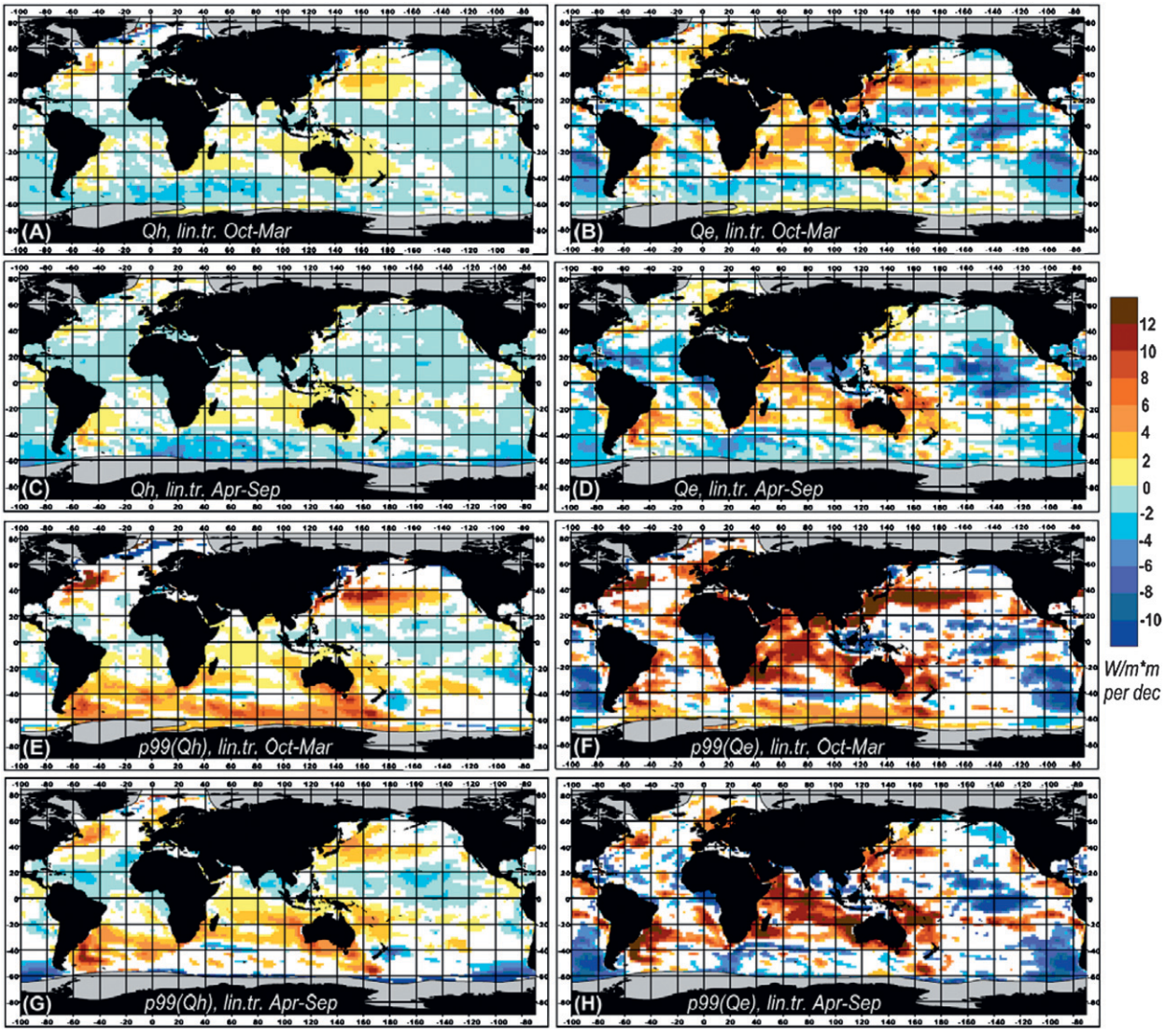

FIG. 11. Linear trends (1948–2008) (W m^{-2} $decade^{-1}$) in the (a)–(d) means and (e)–(h) 99th percentiles of the (left) sensible and (right) latent heat fluxes for the periods from October to March and from April to September. Only trends significant at the 95% level are shown. Statistical significance was estimated according to Student's t test and a Wilcoxon test (Pearson and Hartley 1976). Additionally trends were analyzed with respect to the confidence intervals of the trend significance (the reliability ratio; Hayashi 1982). Only trends satisfying all three criteria at the 95% level were considered to be significant.

typically >1 in the subtropics and tropics. Note, that the higher *relative* sampling error in extreme fluxes compared to the mean flux values does not imply a similar conclusion for the absolute sampling errors, which are the largest in poorly sampled regions outside of the major ship routes (Figs. 14c,d). Figures 14g–j also show estimates of the total sampling errors in the location and scale parameters along with the areas (colored in gray) where they fall within the confident intervals of the parameters themselves (see appendix A), and thus they cannot be discussed with confidence. The largest sampling uncertainties in α (40%–50% of the mean values for α_h and 20%–30% of the mean for α_e) are observed in the tropical areas. In the mid- and subpolar latitudes, sampling errors in α_h and α_e decrease together with the mean values of the parameters and become in many areas smaller than the confident intervals of α. Sampling errors in β_h and β_e also drop considerably in the regions of the Gulf Stream and Kuroshio (for Q_h) and in the Southern Ocean subtropics (for Q_e), where their magnitudes become smaller than the confident intervals.

The impact of sampling on the global air–sea turbulent fluxes is shown in Fig. 15, demonstrating the differences between the two-dimensional distributions of the regularly

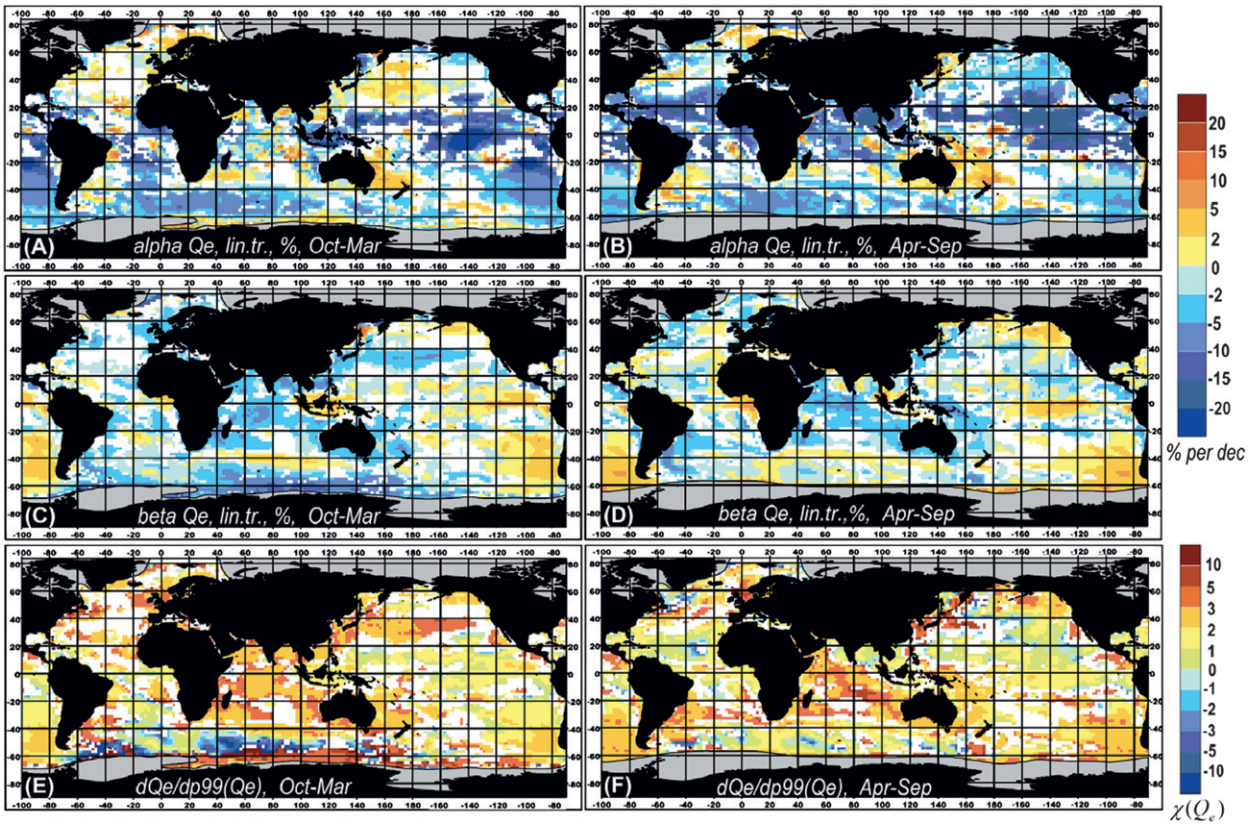

FIG. 12. Linear tendencies in the (top) location and (middle) scale parameters for the latent heat flux (% decade^{-1}) for the periods (a),(c) October–March and (b),(d) April–September, shown only in the locations where the trends in the mean fluxes are statistically significant. (bottom) Ratios (9) between the trends in extreme and mean latent heat fluxes for (e) October–March and (f) April–September.

sampled (Fig. 7) and undersampled fluxes in the coordinates of the location and scale parameters. Gulev et al. (2007a) argued that a *systematic* effect of sampling errors for long-term flux estimates is hardly detectable in most regions. Stormy conditions typically do not result in significant changes in major ship routes but rather affect the quality of the reports. In this respect a significant difference between the random and the total sampling error (Gulev et al. 2007a) can be explained by the fact that the actual sampling is characterized by the grouping of reports in the adjacent series of interdependent observations that reduces the effective number of independent samples. Figures 15a,b show the differences between the occurrences of the regularly sampled and undersampled fluxes at the two-dimensional α–β diagram, computed by subtracting the occurrences of the VOS-like sampled fluxes from the occurrences of the regularly sampled ones. This figure clearly demonstrates that the undersampling tends to shift both location and scale parameters toward somewhat higher values. However, when these changes are not negligible (at least 5%–10% of the mean probabilities shown in Fig. 7), they do not unconditionally imply any systematic decrease or increase of the mean fluxes. At the same time, if we consider these changes with respect to the contours of extreme fluxes at α–β diagram, there will be a clear evidence of the systematically smaller estimates of, for example, 99th percentiles of turbulent heat fluxes in the undersampled subset compared to the fully sampled fluxes. Thus, it is likely that sampling may seriously affect the tails of probability distributions and result in an underestimation of extreme turbulent fluxes.

7. Summary and discussion

We have analyzed the probability distributions of surface turbulent sensible and latent heat fluxes using the two-parametric MFT distribution, which effectively describes statistical properties of turbulent fluxes and fits well with the observed probability of occurrence of fluxes in most areas. Application of the MFT distribution allows us to extend the analysis of mean surface turbulent fluxes to the consideration of the distribution

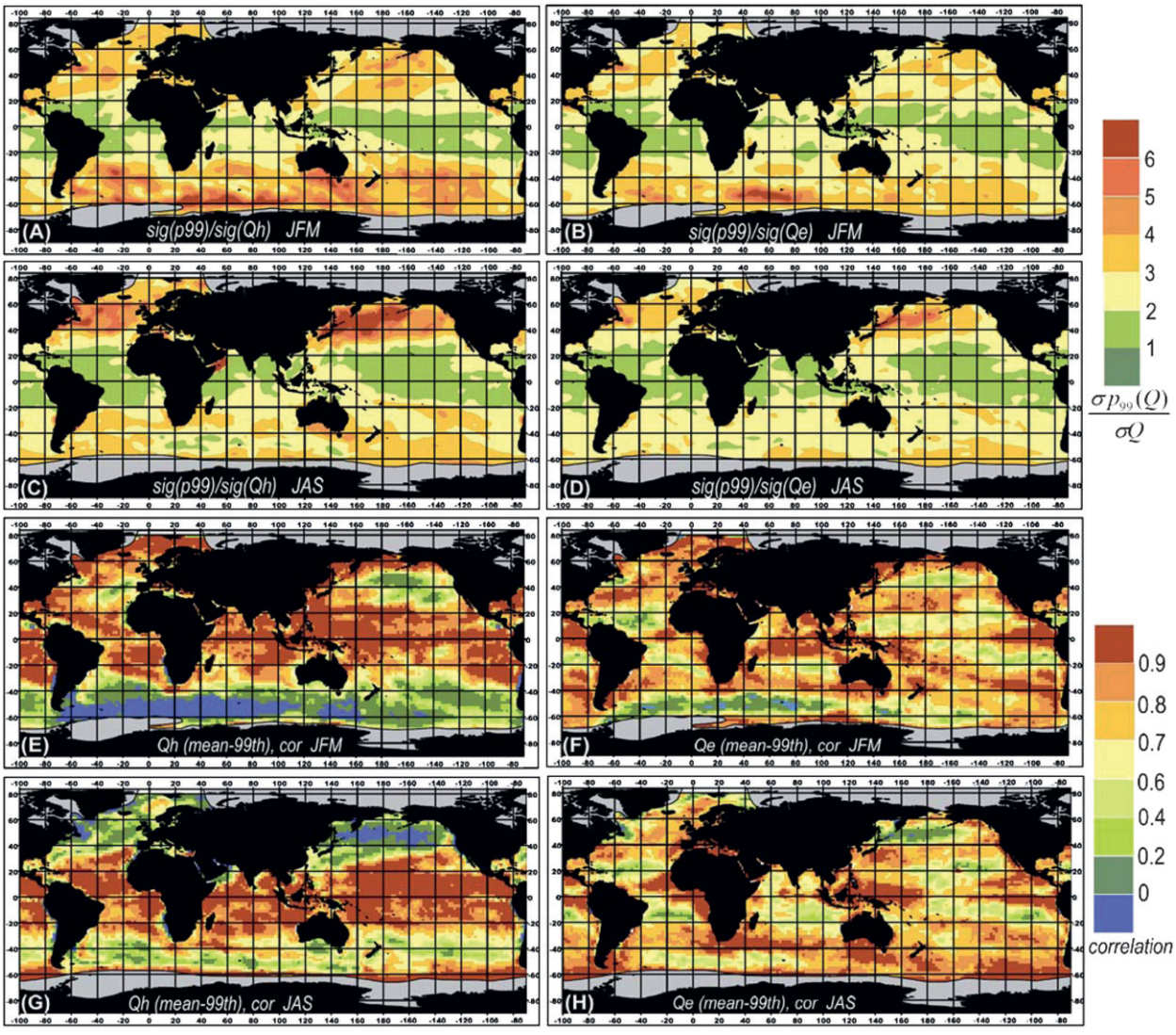

FIG. 13. Ratios between interannual standard deviations of the mean fluxes and their 99th percentiles for (a),(c) Q_h and (b),(d) Q_e for JFM and JAS as well as correlation coefficients between the detrended seasonal anomalies of means and 99th percentiles of the (e),(g) sensible and (f),(h) latent fluxes for JFM and JAS.

parameters (location and scale) and to the quantification of turbulent fluxes of rare occurrences that cannot be always accurately estimated from the raw data. Mean climatology, seasonal and interannual variability of the distribution parameters, and extreme flux values were derived using turbulent fluxes recomputed from the 6-hourly NCEP–NCAR state variables for the period 1948–2008. Extreme sensible and latent fluxes may locally amount to 1500–2000 W m^{-2} (for the 99th percentile) and can exceed 2000 W m^{-2} for the higher percentiles. Our analysis has identified the areas (e.g., tropical regions, Southern Ocean, Kuroshio Extension) where both the linear trends and the interannual variability of the mean and extreme turbulent fluxes are not consistent. Finally, probability density distributions were applied to the analysis of sampling uncertainties in the VOS-based surface flux climatologies. Inadequate sampling results in more than 100 W m^{-2} uncertainties in climatological extreme fluxes, which are twice as large in the cold season. The ratio between the relative sampling errors in extreme and mean fluxes varies significantly over the global ocean, being the largest in the tropics, thus implying that even under the relatively small sampling uncertainties in the means, sampling errors in extreme fluxes may be quite large. Although sampling does not have a visible systematic effect on the estimates of the mean fluxes, it results in a considerable underestimation of extreme fluxes.

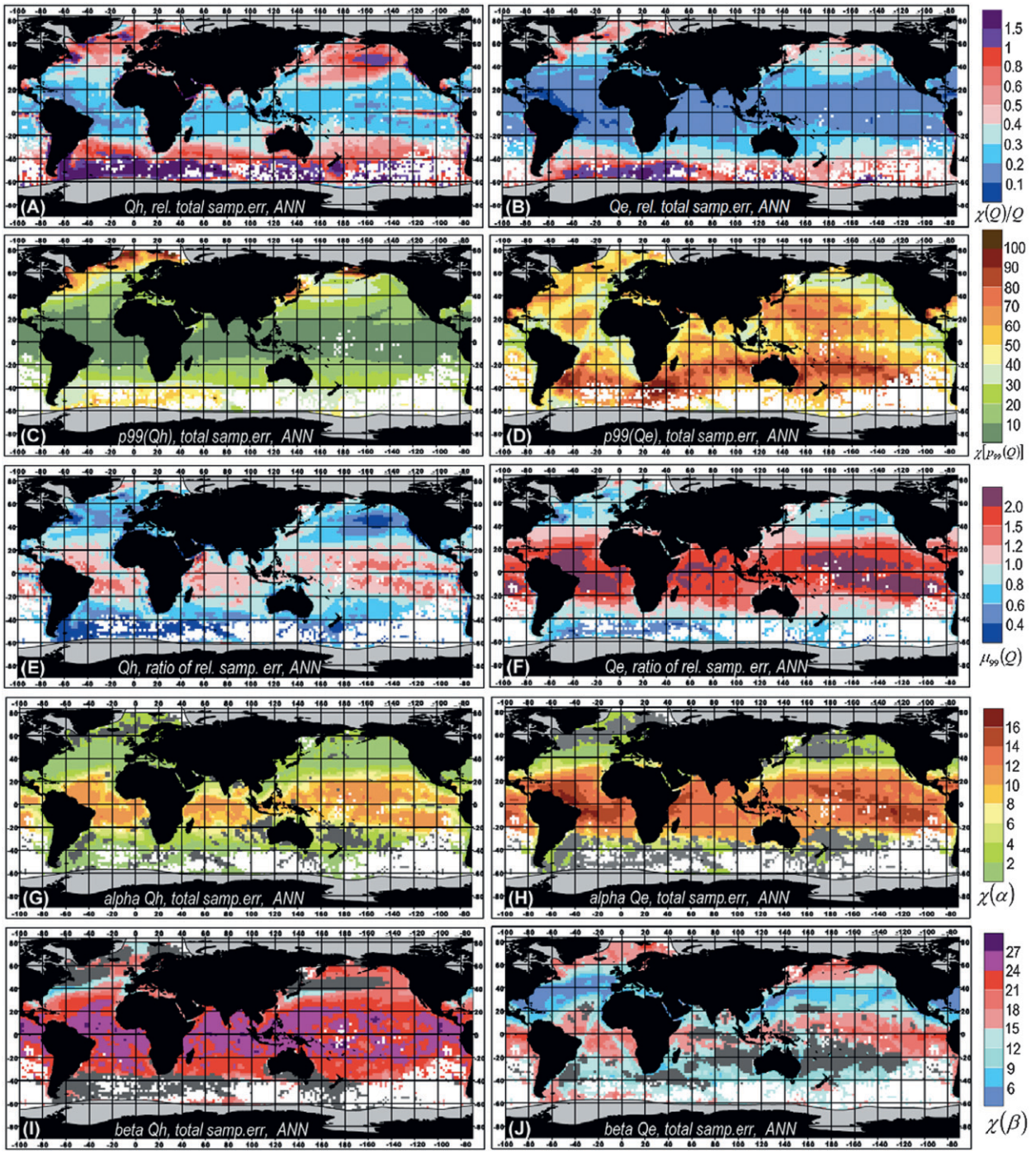

FIG. 14. Total sampling errors in (a) sensible and (b) latent annual mean surface fluxes normalized by the mean surface flux magnitudes, total sampling errors in the 99th percentile of (c) sensible and (d) latent heat fluxes (W m^{-2}), ratio μ (10) between the relative total sampling errors in the extreme and mean fluxes for (e) sensible and (f) latent heat fluxes, and total sampling errors in the (g),(h) location and (i),(j) scale parameters for sensible and latent heat fluxes. Gray shading in (g)–(j) indicates the areas where sampling errors in the MFT parameters are within the confident intervals of the parameters and, thus, cannot be considered to be significant.

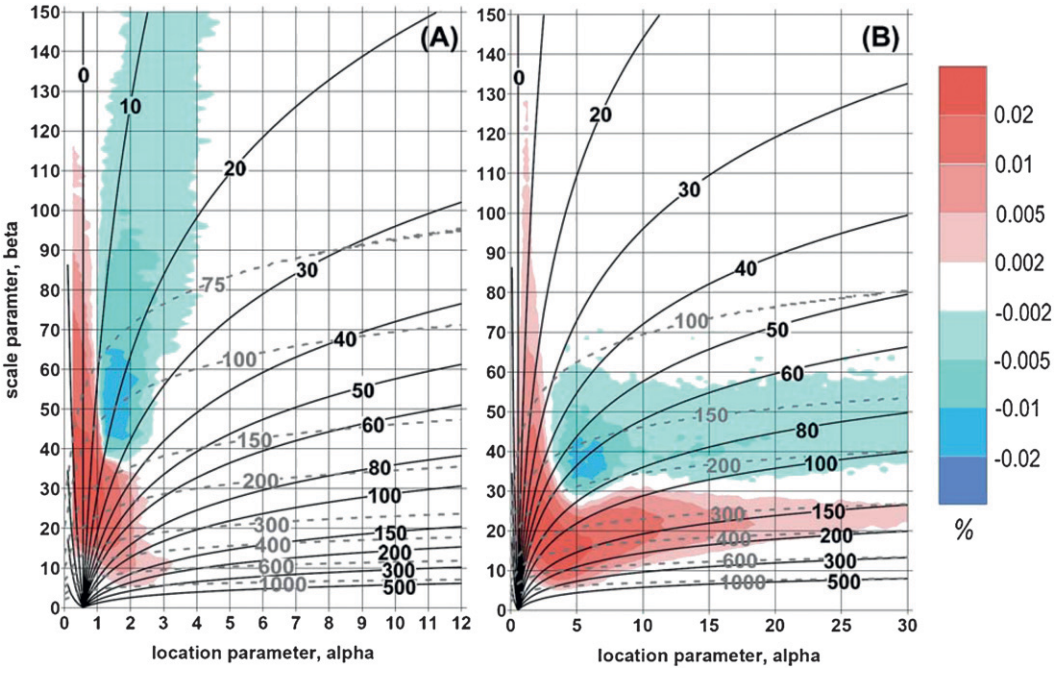

FIG. 15. Differences between the occurrences (%) of the regularly sampled and undersampled fluxes at the 2-dimensional α–β diagram for (a) sensible and (b) latent heat fluxes. Differences were computed by subtracting the occurrences of the VOS-like sampled fluxes from the occurrences of the regularly sampled ones. Black solid contours show mean flux values; gray dashed contours indicate the 99th percentile of fluxes.

Analysis of probability distributions of surface turbulent fluxes enables a number of applications for validating different surface flux products and understanding the variability in surface fluxes. First of all, comparisons of surface flux products from different reanalyses, satellite data, and VOS can move from considering the means and standard deviations to analyzing the parameters of probability distributions and extreme fluxes. Comparisons of surface flux products with each other and their validations against the buoy data typically consider the differences in mean values (e.g., Josey 2001; Smith et al. 2001; Moore and Renfrew 2002; Renfrew et al. 2002; Kubota et al. 2003, 2008; Rouault et al. 2003; Yu et al. 2004a; Liu and Curry 2006; Bouras 2006; Grodsky et al. 2009; Andersson et al. 2011). Smith et al. (2011) extended these comparisons to the consideration of different percentiles (from 5th to 95th), which were estimated from the raw data. However, these estimates may be biased because of a different sampling density in different datasets. Furthermore, raw data do not allow for the estimation of higher percentiles (e.g., 99.99th).

Considering applications of the suggested framework to the intercomparison of different reanalyses, we strongly believe that the analysis of probability distributions may help to quantify skills of different reanalyses to replicate extreme fluxes associated with, for example, tropical cyclones and the other small-scale events, which are only accurately reproduced by the modern era reanalyses. For instance, Schenkel and Hart (2012) demonstrated large differences in maximum wind speed characteristics of tropical cyclones in five reanalyses [40-yr European Centre for Medium-Range Weather Forecasts (ECMWF) Re-Analysis (ERA-40), the ECMWF Interim reanalysis (ERA-Interim), Japanese reanalysis (JRA), Modern-Era Retrospective Analysis for Research and Applications (MERRA), and Climate Forecast System Reanalysis (CFSR)] amounting to more than 20 m s^{-1}. These differences definitely affect estimates of turbulent fluxes and may also have a serious effect on the mean flux values. In this respect, the analysis of PDFs of turbulent fluxes revealed by different reanalyses will provide a good prospect for the intercomparison and validation of reanalysis flux products.

Besides the comparisons of different datasets, analysis of surface flux PDFs may also shed more light on the comparisons between different flux computation schemes, especially in the regions of high occurrence of extreme fluxes (western boundary currents and high latitudes). According to Bourassa and Gille (2008) in the Drake Passage, the probability of sensible heat fluxes exceeding 450 W m^{-2} in winter may vary within 20 times when computed by different schemes. Given that the major uncertainties of the bulk flux algorithms are associated with the strong winds, implying extreme turbulent fluxes (e.g., Gulev et al. 2010), the analysis of PDFs of surface fluxes

derived from different parameterizations may show how different schemes replicate the flux extremes. This will help to quantify the range of comparability of different methods in terms of percentiles of the flux distributions.

Analysis of the parameters of PDFs of surface turbulent fluxes may help to identify the mechanisms responsible for the variability in surface turbulent fluxes in the western boundary current extension regions. Our Figs. 11–13 clearly identify the regions where the trends and the interannual variability between mean and extreme fluxes are not consistent. Trends in extreme fluxes in the western boundary current regions are associated with the growing occurrence of cyclone activity and the associated cold-air outbreaks. In the midlatitudes, especially in wintertime, a series of cyclones are associated with the high occurrences of extreme fluxes in the cyclone rear parts (e.g., Zolina and Gulev 2003; Rudeva and Gulev 2011; Shaman et al. 2010; Bond et al. 2010). Shaman et al. (2010) demonstrated that the growing occurrence of cyclonic events in the Gulf Stream area in winter season (November–March) results in the coordinated increase of both mean and extreme fluxes. In summer season the occurrence of cyclone events provoking high turbulent fluxes is relatively low. Although these very rare events do contribute to the formation of extreme fluxes, mean fluxes may be formed by various mechanisms associated with, for example, the summer monsoon onset in the Kuroshio region, South China Sea, and the Indian Ocean. This may result in different tendencies in mean and extreme fluxes, especially during the warm season. Considering the changes in the mean and extreme fluxes in the midlatitudes, it is likely that even more remarkable disagreements can occur at shorter (e.g., weekly) time scales. When the cyclonic regime is changed to the blocking circulation, the probability distributions may change drastically. Thus, the analysis of changes in cyclone activity provides a potential clue for understanding the mechanisms of climate variability in probability distributions of surface turbulent heat fluxes.

Recently, Konda et al. (2010) analyzed the differences in turbulent fluxes associated with different airmass transformations north and south of the Kuroshio Front. Similar differences were noted by Zolina and Gulev (2003) for the Gulf Stream Front. Strong differences under different directions of wind blow can be easily quantified in terms of the MFT distribution parameters and estimates of fluxes of rare occurrences. We estimated the parameters of the MFT distribution using the Kuroshio Extension Observatory (KEO, south of Kuroshio) and the Japan Agency for Marine-Earth Science and Technology (JAMSTEC) KEO (JKEO, north of Kuroshio) data for the winter periods of 2007 and 2008 analyzed by Konda et al. (2010). Although for the strong northerly winds the difference in the latent heat flux between the two buoys is small, the differences in the location and scale parameters of the MFT distribution are responsible for about a 30% difference in the 99.9th percentile of Q_e (1245 W m^{-2} at the KEO buoy versus 956 W m^{-2} at the JKEO buoy). Thus, what was termed by Konda et al. (2010) as ''extremely large fluxes'' may become quite different north and south of the Kuroshio Front. Under the monsoon conditions in 2007 and 2008, when at the southern KEO buoy the latent fluxes were larger by 40–80 W m^{-2}, the MFT distribution returns very similar extreme fluxes (680 and 697 W m^{-2}, respectively), implying that the difference in the means was caused by the background conditions that are typical for the alongfront wind blow.

Analysis of the PDFs of surface turbulent fluxes also enables a considerable progress in the estimation of sampling uncertainties and their potential minimization. Here we presented only the first results from the analysis of the sampling effects. Further steps will involve the application of the theory of censored samples, which generally allows (under some assumptions) for the correction of the parameters of distributions derived from the undersampled data and, thus, to minimize sampling biases in the mean fluxes and their statistics. For the development of the appropriate algorithms, however, it is necessary to investigate the statistical relationships between the sampling-implied biases in MFT distribution parameters and the magnitudes of synoptic and mesoscale variability. These relationships can vary significantly from one region to another, and their accurate regional estimates are required. If sampling uncertainties are quantified in terms of MFT distribution parameters, this may help to compare the satellite, VOS, and reanalysis products more accurately; they all have different sampling that affect the products; and sampling-associated uncertainties may be regionally comparable to those attributed to the parameterizations and retrieval algorithms.

Acknowledgments. A considerable part of this study was accomplished during SKG's periodical visits to IFM-GEOMAR. SKG thanks IFM-GEOMAR for its hospitality and AvH-Stiftung for funding the visits. Discussions with Mark Bourassa and Carol Anne Clayson of FSU (Tallahassee) are appreciated. We thank Scott Woodruff of the NOAA Earth System Research Laboratory (ESRL) (Boulder) and Steve Worley of DSS of NCAR (Boulder) for their many years of reliable feedback on the ICOADS data provision. Suggestions and criticism from the three anonymous reviewers have greatly contributed to the improvement of the manuscript. This work was supported by the Ministry of Education and Science of the Russian Federation under the World Ocean National Programme (Contract 01.420.1.2.0001), Russian Foundation for Basic Research (Grant 11-05-00253-a),

and a special grant from the Ministry of Education and Science of the Russian Federation for establishing excellence in science at Russian universities.

APPENDIX A

Estimation of the Confidence Limits for the Parameters of MFT Distribution

Equations (7) provide the maximum likelihood estimation of the parameters of MFT distribution, that is, the maximum of the likelihood function, as follows:

$$p(\mathbf{x},\alpha,\beta) = (\alpha\beta)^n \exp\left(-\beta\sum_{i=1}^{n} x_i\right)\exp\left[-\alpha\sum_{i=1}^{n}\exp(-\beta x_i)\right]. \tag{A1}$$

For the logarithm of (A1), the following equality holds:

$$\Lambda = \ln[p(\overline{x},\alpha,\beta)] = n\ln(\beta) + n\ln(\alpha) - \beta\sum_{i=1}^{n} x_i - \alpha\sum_{i=1}^{n}\exp(-\beta x_i), \tag{A2}$$

where n is the number of observations, $\mathbf{x} = (x_1, \ldots x_n)$ is the vector of flux values, $p(\mathbf{x}, \alpha, \beta)$ stands for the density of the joint distribution of the vector of flux values, and L denotes $\ln[p(\overline{x},\alpha,\beta)]$ for brevity. Applying a standard mathematical technique, we can prove that if all values in the vector $\mathbf{x} = (x_1, \ldots x_n)$ are not identical, the equations in (7) have the root $\alpha_* > 0, \beta_* > 0$ and that this root will be unique at the interval $0 < \alpha < \infty$, $0 < \beta < \infty$.

In this case the vector $\sqrt{n}(\alpha - \alpha_*, \beta - \beta_*)$ is distributed asymptotically (when $n \to \infty$) as a two-dimensional Gaussian vector with zero mean and covariance matrix $\mathbf{I}^{-1}(\alpha_*, \beta_*)$, where $\mathbf{I}$ is the observed information matrix and $\mathbf{I}^{-1}(\alpha_*, \beta_*)$ is its inverted matrix with the matrix elements being

$$i_{11} = \frac{\partial^2\Lambda}{\partial\alpha^2} = -\frac{n}{\alpha^2}, \quad i_{22} = \frac{\partial^2\Lambda}{\partial\beta^2} = \frac{n}{\beta^2} - \alpha\sum_{j=1}^{n} x_j^2 e^{-\beta x_j},$$

$$i_{12} = i_{21} = \frac{\partial^2\Lambda}{\partial\alpha\partial\beta} = -\sum_{j=1}^{n} x_j e^{-\beta x_j}. \tag{A3}$$

The proof of this statement follows from a general statement for the regular distributions (see, e.g., Lehmann and Romano 2005) and from the regularity of the considered distribution. As a corollary of this statement, the confident intervals for parameters α and β with a 95% significance level will be given as an internal domain of the ellipse as follows:

$$\frac{(\alpha-\alpha_*)^2}{\sigma_1^2} - \frac{2\rho}{\sigma_1\sigma_2}(\alpha-\alpha_*)(\beta-\beta_*) + \frac{(\beta-\beta_*)^2}{\sigma_2^2} = 6(1-\rho^2), \tag{A4}$$

where $\sigma_1^2 = i_{11}, \sigma_2^2 = i_{22}$, and $\rho = i_{12}/\sigma_1\sigma_2$ at points ($\alpha = \alpha_*, \beta = \beta_*$). By the consecutive replacement of variables in (A4), this ellipse can be transited into a canonic form as follows:

$$\left[\frac{u}{\sqrt{3(1+\rho)}}\right]^2 + \left[\frac{v}{\sqrt{3(1+\rho)}}\right]^2 = 1 \tag{A5}$$

and rewritten in a parametric form as

$$u = \sqrt{3(1+\rho)}\cos\phi, \quad v = \sqrt{3(1+\rho)}\sin\phi. \tag{A6}$$

Returning to the original variables, we obtain the final parametric expression as follows:

$$\alpha = R\sigma_1(\sin\varphi + \cos\varphi) + \alpha_* \quad \text{and}$$
$$\beta = R\sigma_2(\cos\varphi - \sin\varphi) + \beta_*, \tag{A7}$$

where

$$R = \sqrt{3(1+\rho)} \tag{A8}$$

and φ varies from 0 to 2π. This expression (A7) was used for the estimation of confident intervals for α and β.

APPENDIX B

Testing the Applicability of the MFT with Respect to the Alternative Distributions Using Neyman–Pearson Criterion

The null hypothesis (H0) is that the turbulent flux (x) implies the MFT distribution, given by

$$p_0(\mathbf{x},\alpha,\beta) = \prod_{i=1}^{n}\alpha\beta\exp(-\beta x_i)\exp[-\alpha\exp(-\beta x_i)], \tag{B1}$$

where n is the number of observations (sample size) and i is the current index of samples. The competitive hypothesis (H1, being an alternative to H0) is that x has a three-parameter Weibull distribution as follows:

$$p_1(\mathbf{x},\kappa,\lambda,\theta) = \prod_{i=1}^{n}\frac{k}{\lambda}\left(\frac{x_i-\theta}{\lambda}\right)^{k-1}\exp\left[-\left(\frac{x_i-\theta}{\lambda}\right)^{k}\right], \tag{B2}$$

with θ, κ, and λ being location, shape, and scale parameters, respectively. According to the Neyman–Pearson theorem (Borowkov 1984), the most powerful criterion for testing the hypothesis H0 with respect to H1 is based on the following statistics:

$$L = \ln\frac{p_1}{p_0} = \sum_{i-1}^{n}\ln\left[\frac{k}{\lambda}\left(\frac{x_i-\theta}{\lambda}\right)^{k-1}\right]\exp\left[-\left(\frac{x-\theta}{\lambda}\right)^{k}\right] - \sum_{i=1}^{n}\ln\{\alpha\beta\exp(-\beta x)\exp[-\alpha\exp(-\beta x)]\}. \tag{B3}$$

The H0 hypothesis is rejected if the probability

$$P_{\mathrm{H0}}\left(\ln\frac{p_1}{p_0}\right) > \varepsilon, \tag{B4}$$

where ε is the p value corresponding to the chosen significance level (e.g., 95% or 99%). Although the direct computation of statistics L in (B3) is quite complicated, we can note that all random values x_i, $i = 1, \ldots, n$ are independent and identically distributed. Therefore, all the sums in (B3) will asymptotically have a Gaussian distribution with the mean value $n\mu$ and the variance being $n\sigma^2$, where

$$\mu = \int_{-\infty}^{\infty}\ln\left[\frac{P_1(x)}{P_0(x)}\right]P_0(x)\,dx \quad \text{and}$$
$$\sigma^2 = \int_{-\infty}^{\infty}\ln^2\left[\frac{P_1(x)}{P_0(x)}\right]P_0(x)\,dx - \mu^2, \ \text{respectively,} \tag{B5}$$

where

$$P_1(x) = \kappa\lambda^{-\kappa}\exp[\lambda^{-\kappa}(x-\theta)^{\kappa}] \quad \text{and}$$
$$P_0(x) = \alpha\beta\exp(-\beta x)\exp[-\alpha\exp(-\beta x)] \tag{B6}$$

are the PDFs of the Weibull and the MFT distribution, respectively. Now, substituting parameters α, β, θ, κ, and λ and computing $n\mu$, $n\sigma^2$ we can define the actual value of statistics L and test the hypothesis H0. According to (B4), the hypothesis will be rejected if L is greater than p value ε at a given level of significance. A formulation similar to (B2)–(B5) can be developed for the Fréchet distribution.

REFERENCES

Akima, H., 1970: A new method of interpolation and smooth curve fitting based on local procedures. *J. Assoc. Comput. Mach.,* **17,** 589–602.

Andersson, A., C. Klepp, K. Fennig, S. Bakan, H. Grassl, and J. Schulz, 2011: Evaluation of HOAPS-3 ocean surface freshwater flux components. *J. Appl. Meteor. Climatol.,* **50,** 379–398.

Bazant, M. Z., 2000: Largest cluster in subcritical percolation. *Phys. Rev. E,* **62,** 1660–1669.

Bedacht, E., S. K. Gulev, and A. Macke, 2007: Intercomparison of global cloud cover fields over oceans from the VOS observations and NCEP/NCAR reanalysis. *Int. J. Climatol.,* **27,** 1707–1719, doi:10.1002/joc.1490.

Bentamy, A., K. B. Katsaros, A. M. Mestas-Nuñez, W. M. Drennan, E. B. Forde, and H. Roquet, 2003: Satellite estimates of wind speed and latent heat flux over the global oceans. *J. Climate,* **16,** 637–656.

Berry, D. I., and E. C. Kent, 2009: A new air–sea interaction gridded dataset from ICOADS with uncertainty estimates. *Bull. Amer. Meteor. Soc.,* **90,** 645–656.

Besset, D. H., 2001: *Object-Oriented Implementation of Numerical Methods: An Introduction with Java and Smalltalk*. Morgan Kaufmann Publishers, 766 pp.

Bhavsar, S. P., and J. D. Barrow, 1985: First ranked galaxies in groups and clusters. *Mon. Not. Roy. Astron. Soc.,* **213,** 857–869.

Bond, N. A., and M. F. Cronin, 2008: Regional weather patterns during anomalous air–sea fluxes at the Kuroshio Extension Observatory (KEO). *J. Climate,* **21,** 1680–1697.

——, ——, and M. Garvert, 2010: Atmospheric sensitivity to SST near the Kuroshio Extension during the extratropical transition of Typhoon Tokage. *Mon. Wea. Rev.,* **138,** 2644–2663.

Borowkov, A. A., 1984: *Mathematical Statistics*. Nauka, 472 pp.

Bouras, D., 2006: Comparison of five satellite-derived latent heat flux products to moored buoy data. *J. Climate,* **19,** 6291–6313.

Bourassa, M., and S. Gille, 2008: US CLIVAR Working Group on high latitude surface fluxes. *Variations,* **6** (1), 8–11.

Brohan, P., J. Kennedy, I. Harris, S. F. B. Tett, and P. D. Jones, 2006: Uncertainty estimates in regional and global observed temperature changes: A new dataset from 1850. *J. Geophys. Res.,* **111,** D12106, doi:10.1029/2005JD006548.

Brunke, M. A., C. W. Fairall, X. Zeng, L. Eymard, and J. A. Curry, 2003: Which bulk aerodynamic algorithms are least problematic in computing ocean surface turbulent fluxes? *J. Climate,* **16,** 619–635.

Cayan, D., 1992: Variability of latent and sensible heat fluxes estimated using bulk formulae. *Atmos.–Ocean,* **30,** 1–42.

Chang, E. K. M., 2005: Effects of secular changes in frequency of observations and observational errors on monthly mean MSLP summary statistics derived from ICOADS. *J. Climate,* **18,** 3623–3633.

——, 2007: Assessing the increasing trend in Northern Hemisphere winter storm track activity using surface ship observations and a statistical storm track model. *J. Climate,* **20,** 5607–5628.

Chou, S. H., E. Nelkin, J. Ardizzone, and R. M. Atlas, 2004: A comparison of latent heat fluxes over global oceans for four flux products. *J. Climate,* **17,** 3973–3989.

Coles, S. G., 1989: On goodness-of-fit tests for the two-parameter Weibull distribution derived from stabilized probability plot. *Biometrika,* **76,** 593–598.

D'Agostino, R. B., and M. A. Stephens, Eds.,1986: *Goodness-of-Fit Techniques*. Statistics: Textbooks and Monographs, Vol. 68, Marcel Dekker, 560 pp.

Fairall, C. W., E. F. Bradly, J. E. Hare, A. A. Grachev, and J. B. Edson, 2003: Bulk parameterization of air–sea fluxes: Updates and verification for the COARE algorithm. *J. Climate,* **16,** 571–591.

Gleckler, P., and B. Weare, 1997: Uncertainties in global ocean surface heat flux climatologies derived from ship observations. *J. Climate,* **10,** 2764–2781.

Grist, J. R., and S. A. Josey, 2003: Inverse analysis adjustment of the SOC air–sea flux climatology using ocean heat transport constraints. *J. Climate,* **16,** 3274–3295.

Grodsky, S. A., A. Bentamy, J. A. Carton, and R. T. Pinker, 2009: Intraseasonal latent heat flux based on satellite observations. *J. Climate,* **22,** 4539–4556.

Gulev, S. K., V. Grigorieva, A. Sterl, and D. Woolf, 2003: Assessment of the reliability of wave observations from voluntary observing ships: Insights from the validation of a global wind wave climatology based on voluntary observing ship data. *J. Geophys. Res.,* **108,** 3236, doi:10.1029/2002JC001437.

——, T. Jung, and E. Ruprecht, 2007a: Estimation of the impact of sampling errors in the VOS observations on air–sea fluxes. Part I: Uncertainties in climate means. *J. Climate,* **20,** 279–301.

——, ——, and ——, 2007b: Estimation of the impact of sampling errors in the VOS observations on air–sea fluxes. Part II: Impact on trends and interannual variability. *J. Climate,* **20,** 302–315.

——, and Coauthors, 2010: Surface energy, CO_2 fluxes and sea ice. *Proceedings of OceanObs'09: Sustained Ocean Observations and Information for Society,* Vol. 1, J. Hall, D. E. Harrison, and D. Stammer, Eds., ESA Publ. WPP-306, 19 pp.

Hayashi, Y., 1982: Confidence intervals of a climatic signal. *J. Atmos. Sci.,* **39,** 1895–1905.

Isemer, H.-J., and L. Hasse, 1991: The scientific Beaufort equivalent scale: Effects on wind statistics and climatological air–sea flux estimates in the North Atlantic Ocean. *J. Climate,* **4,** 819–836.

Josey, S. A., 2001: A comparison of ECMWF, NCEP–NCAR, and SOC surface heat fluxes with moored buoy measurements in the subduction region of the northeast Atlantic. *J. Climate,* **14,** 1780–1789.

——, E. C. Kent, and P. K. Taylor, 1999: New insights into the ocean heat budget closure problem from analysis of the SOC air–sea flux climatology. *J. Climate,* **12,** 2856–2880.

Kalnay, E., and Coauthors, 1996: The NCEP/NCAR 40-Year Reanalysis Project. *Bull. Amer. Meteor. Soc.,* **77,** 437–471.

Kaplan, A., M. A. Cane, and Y. Kushnir, 2003: Reduced space approach to the optimal analysis of historical marine observations: Accomplishments, difficulties, and prospects. Advances in the applications of marine climatology: The dynamic part of the WMO guide to the applications of marine meteorology, WMO Tech. Doc. WMO/TD-1081, JCOMM Tech. Rep. 13, 199–216.

Kent, E. C., and D. I. Berry, 2005: Quantifying random measurement errors in voluntary observing ships' meteorological observations. *Int. J. Climatol.,* **25,** 843–856, doi:10.1002/joc.1167.

——, P. K. Taylor, and P. Challenor, 2000: The effect of successive correction on variability estimates for climatological datasets. *J. Climate,* **13,** 1845–1857.

——, S. D. Woodruff, and D. I. Berry, 2007: Metadata from WMO Publication No. 47 and an assessment of Voluntary Observing Ship observation heights in ICOADS. *J. Atmos. Oceanic Technol.,* **24,** 214–234.

Kistler, R., and Coauthors, 2001: The NCEP–NCAR 50-Year Reanalysis: Monthly means CD-ROM and documentation. *Bull. Amer. Meteor. Soc.,* **82,** 247–267.

Konda, M., H. Ichikawa, H. Tomita, and M. F. Cronin, 2010: Surface heat flux variations across the Kuroshio Extension as observed by surface flux buoys. *J. Climate,* **23,** 5206–5221.

Kubota, M., A. Kano, H. Muramatsu, and H. Tomita, 2003: Intercomparison of various surface latent heat flux fields. *J. Climate,* **16,** 670–678.

——, N. Iwabe, M. F. Cronin, and H. Tomita, 2008: Surface heat fluxes from the NCEP/NCAR and NCEP/DOE reanalyses at the Kuroshio Extension Observatory buoy site. *J. Geophys. Res.,* **113,** C02009, doi:10.1029/2007JC004338.

LabSea Group, 1998: The Labrador Sea Deep Convection Experiment. *Bull. Amer. Meteor. Soc.,* **79,** 2033–2058.

Large, W. G., and S. G. Yeager, 2009: The global climatology of an interannually varying air–sea flux data set. *Climate Dyn.,* **33,** 341–364, doi:10.1007/s00382-008-0441-3.

Legler, D., 1991: Errors in five-day mean surface wind and temperature conditions due to inadequate sampling. *J. Atmos. Oceanic Technol.,* **8,** 705–712.

Lehmann, E. L., and J. P. Romano, 2005: *Testing Statistical Hypotheses*. 3rd ed. Springer, 784 pp.

Littell, R. C., J. T. McClave, and W. W. Offen, 1979: Goodness-of-fit tests for the two parameter Weibull distribution. *Commun. Stat.,* **8B,** 257–269.

Liu, J., and J. A. Curry, 2006: Variability of the tropical and subtropical ocean surface latent heat flux during 1989–2000. *Geophys. Res. Lett.,* **33,** L05706, doi:10.1029/2005GL024809.

Lo, A. K., and G. A. McBean, 1978: On the relative errors in methods of flux calculations. *J. Appl. Meteor.,* **17,** 1704–1711.

Michael, J. R., 1983: The stabilized probability plot. *Biometrika,* **70,** 11–17.

Monahan, A. H., 2006a: The probability distribution of sea surface wind speeds. Part I: Theory and sea winds observations. *J. Climate,* **19,** 497–520.

——, 2006b: The probability distribution of sea surface wind speeds. Part II: Dataset intercomparison and seasonal variability. *J. Climate,* **19,** 521–534.

——, 2007: Empirical models of the probability distribution of sea surface wind speeds. *J. Climate,* **20,** 5798–5814.

Moore, G. W. K., and I. A. Renfrew, 2002: An assessment of the surface turbulent heat fluxes from the NCEP–NCAR reanalysis over the western boundary currents. *J. Climate,* **15,** 2020–2037.

Morrissey, M. L., A. Albers, J. S. Greene, and S. Postawko, 2010: An isofactorial change-of-scale model for the wind speed probability density function. *J. Atmos. Oceanic Technol.,* **27,** 257–273.

Pearson, E. S., and H. O. Hartley, Eds., 1976: *Biometrika Tables for Statisticians*. Vol. 2. Biometrika Trust, 226 pp.

Ramesh Kumar, M. R., S. Sankar, K. Fennig, D. S. Pai, and J. Schulz, 2005: Air-sea interaction over the Indian Ocean during the contrasting monsoon years 2002 and 2003. *Geophys. Res. Lett.,* **32,** L14821, doi:10.1029/2005GL022587.

——, R. Krishnan, S. Sankar, A. S. Unnikrishnan, and D. S. Pai, 2009: Increasing trend of ''break-monsoon'' conditions over India—Role of ocean–atmosphere processes in the Indian Ocean. *IEEE Geosci. Remote Sens. Lett.,* **6,** 332–336.

Renfrew, I. A., G. W. K. Moore, P. S. Guest, and K. Bumke, 2002: A comparison of surface layer and surface turbulent flux observations over the Labrador Sea with ECMWF analyses and NCEP reanalyses. *J. Phys. Oceanogr.,* **32,** 383–400.

Romanou, A., W. B. Rossow, and S.-H. Chou, 2006: Decorrelation scales of high-resolution turbulent fluxes at the ocean surface and a method to fill in gaps in satellite data products. *J. Climate,* **19,** 3378–3393.

Rouault, M., C. J. C. Reason, J. R. E. Lutjeharms, and A. C. M. Beljaars, 2003: Underestimation of latent and sensible heat fluxes above the Agulhas Current in NCEP and ECMWF analyses. *J. Climate,* **16,** 776–782.

Rudeva, I. A., and S. K. Gulev, 2011: Composite analysis of North Atlantic extratropical cyclones in NCEP–NCAR reanalysis data. *Mon. Wea. Rev.,* **139,** 1419–1446.

Sayama, S., and H. Sekine, 2001: Weibull, log-Weibull and K-distributed ground clutter modeling analyzed by AIC. *IEEE Trans. Aerosp. Electron. Syst.,* **37,** 1108–1113.

Schenkel, B., and R. Hart, 2012: An examination of tropical cyclone position and intensity differences within atmospheric reanalysis datasets. *J. Climate,* in press.

Shaman, J., R. M. Samelson, and E. Skyllingstad, 2010: Air–sea fluxes over the Gulf Stream region: Atmospheric controls and trends. *J. Climate,* **23,** 2651–2670.

Smith, S. R., D. M. Legler, and K. V. Verzone, 2001: Quantifying uncertainties in NCEP reanalyses using high-quality research vessel observations. *J. Climate,* **14,** 4062–4072.

——, P. J. Hughes, and M. A. Bourassa, 2011: A comparison of nine monthly air–sea flux products. *Int. J. Climatol.,* **31,** 1002–1027, doi:10.1002/joc.2225.

Smith, T. M., and R. W. Reynolds, 2004: Improved extended reconstruction of SST (1854–1997). *J. Climate,* **17,** 2466–2477.

Sterl, A., 2001: On the accuracy of gap-filling algorithms in global surface fields. *Geophys. Res. Lett.,* **28,** 2473–2476.

——, 2004: On the (in)homogeneity of reanalysis products. *J. Climate,* **17,** 3866–3873.

Tomita, H., M. Kubota, M. F. Cronin, S. Iwasaki, M. Konda, and H. Ichikawa, 2010: An assessment of surface heat fluxes from J-OFURO2 at the KEO and JKEO sites. *J. Geophys. Res.,* **115,** C03018, doi:10.1029/2009JC005545.

Weare, B. C., 1989: Uncertainties in estimates of surface heat fluxes derived from marine reports over the tropical and subtropical oceans. *Tellus,* **41A,** 357–370.

——, and P. T. Strub, 1981: The significance of sampling biases on calculated monthly mean oceanic surface heat fluxes. *Tellus,* **33,** 211–224.

WGASF Group, 2000: Intercomparison and validation of ocean-atmosphere energy flux fields. Final Rep. of the Joint WCRP/SCOR Working Group on Air-Sea Fluxes (SCOR Working Group 110), P. K. Taylor, Ed., WMO/TD-1036, WCRP Rep. 112, 305 pp. [Available online at http://www.noc.soton.ac.uk/ooc/WGASF/get_report.html.]

White, G. H., 2000: Long-term trends in the NCEP/NCAR reanalysis. *Proc. Second Int. Conf. on Reanalyses,* Reading, United Kingdom, ECMWF, WCRP-109, WMO Tech. Doc. WMO/TD-985, 54–57.

Woodruff, S. D., and Coauthors, 2011: ICOADS release 2.5: Extensions and enhancements to the surface marine meteorological archive. *Int. J. Climatol.,* **31,** 951–967, doi:10.1002/joc.2103.

Worley, S. J., S. D. Woodruff, R. W. Reynolds, S. J. Lubker, and N. Lott, 2005: ICOADS release 2.1 data and products. *Int. J. Climatol.,* **25,** 823–842, doi:10.1002/joc.1166.

Wright, D. G., and K. R. Thompson, 1983: Time-averaged forms of the nonlinear stress law. *J. Phys. Oceanogr.,* **13,** 341–345.

Yau, M. K., and M. Jean, 1989: Synoptic aspects and physical processes in the rapidly intensifying cyclone of 6–8 March 1986. *Atmos.–Ocean,* **27,** 59–86.

Yu, L., 2007: Global variations in oceanic evaporation (1958–2005): The role of the changing wind speed. *J. Climate,* **20,** 5376–5390.

——, and R. A. Weller, 2007: Objectively analyzed air–sea heat fluxes for the global ice-free oceans (1981–2005). *Bull. Amer. Meteor. Soc.,* **88,** 527–539.

——, ——, and B. Sun, 2004a: Improving latent and sensible heat flux estimates for the Atlantic Ocean (1988–99) by a synthesis approach. *J. Climate,* **17,** 373–393.

——, ——, and ——, 2004b: Mean and variability of the WHOI daily latent and sensible heat fluxes at in situ flux measurement sites in the Atlantic Ocean. *J. Climate,* **17,** 2096–2118.

Zolina, O., and S. K. Gulev, 2003: Synoptic variability of ocean–atmosphere turbulent fluxes associated with atmospheric cyclones. *J. Climate,* **16,** 2717–2734.